Inorg. Chem. **2007**, *46*, 9003–9016

Inorganic Chemistry
Article

Tridentate Facial Ligation of Tris(pyridine-2-aldoximato)nickel(II) and Tris(imidazole-2-aldoximato)nickel(II) To Generate $Ni^{II}Fe^{III}Ni^{II}$, $Mn^{III}Ni^{II}$, $Ni^{II}Ni^{II}$, and $Zn^{II}Ni^{II}$ and the Electrooxidized $Mn^{IV}Ni^{II}$, $Ni^{II}Ni^{III}$, and $Zn^{II}Ni^{III}$ Species: A Magnetostructural, Electrochemical, and EPR Spectroscopic Study

Phalguni Chaudhuri,* Thomas Weyhermüller, Rita Wagner, Sumit Khanra, Biplab Biswas, Eberhard Bothe, and Eckhard Bill

Max-Planck-Institut für Bioanorganische Chemie, Stiftstrasse 34-36,
D-45470 Mülheim an der Ruhr, Germany

Received June 1, 2007

Eight hetero- and homometal complexes **1**–**6**, containing the metal centers $Ni^{II}Fe^{III}Ni^{II}$ (**1**), $Mn^{III}Ni^{II}$ (**2**), $Ni^{II}Ni^{II}$ (**3a**–**c** and **4**), $Zn^{II}Ni^{II}$ (**5**), and $Zn^{II}Zn^{II}$ (**6**), are described. The tridentate ligation property of the metal complexes tris-(pyridine-2-aldoximato)nickel(II) and tris(1-methylimidazole-2-aldoximato)nickel(II) with three facially disposed pendent oxime O atoms has been utilized to generate the said complexes. Complex **1** contains metal centers in a linear arrangement, as is revealed by X-ray diffraction. Complexes were characterized by various physical methods including cyclic voltammetry (CV), variable-temperature (2–290 K) magnetic susceptibility, electron paramagnetic resonance (EPR) measurements, and X-ray diffraction methods. Binuclear complexes **2**–**6** are isostructural in the sense that they all contain a metal ion in a distorted octahedral environment MN_3O_3 and a second six-coordinated Ni^{II} ion in a trigonally distorted octahedral NiN_6 geometry. Complexes **1**–**4** display antiferromagnetic exchange coupling of the neighboring metal centers. The order of the strength of exchange coupling in the isostructural Ni^{II}_2 complexes, **3a**–**c**, and **4**, demonstrates the effects of the remote substituents on the spin coupling. The electrochemical measurements CV and square wave voltammograms (SQW) reveal two reversible metal-centered oxidations, which have been assigned to the Ni center ligated to the oxime N atoms, unless a Mn ion is present. Complex **2**, $Mn^{III}Ni^{II}$, exhibits a reduction of Mn^{III} to Mn^{II} and two subsequent oxidations of Mn^{III} and Ni^{II} to the corresponding higher states. These assignments of the redox processes have been complemented by the X-band EPR measurements. That the electrooxidized species [**3a**]$^+$, [**3b**]$^+$, [**3c**]$^+$, and [**4**]$^+$ contain the localized mixed-valent $Ni^{II}Ni^{III}$ system resulting from the spin coupling, a spin quartet ground state, $S_t = {}^3/_2$, has been confirmed by the X-band EPR measurements.

Introduction

The study of spin−spin interactions between paramagnetic metal centers through multiatom bridges is one of the most active research fields in inorganic chemistry because of its relevance to different apparent dissimilar fields like bioinorganic chemistry[1] and molecular magnetism.[2,3] We have been interested in such interactions, particularly involving heterometal complexes[4−12] with the help of suitably designed

---

* To whom correspondence should be addressed. E-mail: chaudhuri@mpi-muelheim.mpg.de.

(1) For example, see: (a) Holm, R. H., Solomon, E. I., Guest Eds. *Chem. Rev.* **1996**, *96* (7); **2004**, *104* (2). (b) Lippard, S. J.; Berg, J. M. *Principles of Bioinorganic Chemistry*; University Science Books: Mill Valley, CA, 1994. (c) Kaim, W.; Schwederski, B. *Bioanorganische Chemie*: B. G. Teubner: Stuttgart, Germany, 1991. (d) *Bioinorganic Chemistry of Copper*; Karlin, K. D., Tyeklár, Z., Eds.; Chapman & Hall: New York, 1993. (e) *Mechanistic Bioinorganic Chemistry*; Holden Thorp, H., Pecoraro, V. L., Eds.; American Chemical Society: Washington, DC, 1995.

(2) (a) *Magneto-Structural Correlations in Exchange Coupled Systems*; Willett, R. D., Gatteschi, D., Kahn, O., Eds.; Kluwer Academic Publishers: Dordrecht, The Netherlands, 1985. (b) *Magnetic Molecular Materials*; Gatteschi, D., Kahn, O., Miller, J. S., Palacio, F., Eds.; Kluwer Academic Publishers: Dordrecht, The Netherlands, 1991. (c) A tribute to Olivier Kahn: *J. Solid State Chem.* **2001**, *159* (No. 2), July.

(3) Kahn, O. *Molecular Magnetism*; VCH-Verlagsgesellschaft: Weinheim, Germany, 1993.

10.1021/ic701073j CCC: $37.00

Chart 1

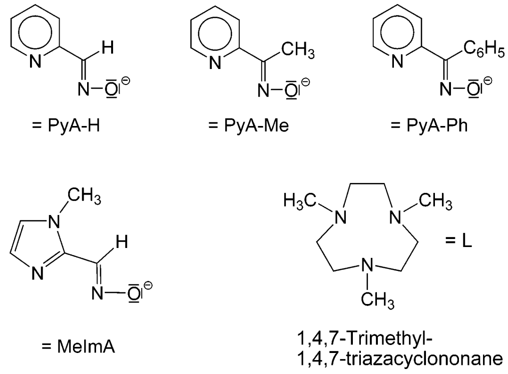

metal oximates as ligands. This work forms part of our program on exchange-coupled oximate-based heteropolymetal systems[13] and deals specifically with the ligation property of derivatives of tris(pyridine-2-aldoximato)nickel(II),[4] $[Ni(PyA\text{-}R)_3]^-$, and of tris(1-methylimidazole-2-aldoximato)nickel(II), $[Ni(MeImA)_3]^-$ (Chart 1).

We were prompted to study the coordination chemistry of these metal complexes as ligands because of the opportunity for their facile in situ formation dictated by the thermodynamic stability of the resulting monoanion containing three facially disposed pendent oxime O atoms for ligation.

In this paper, we explore the ability of $[Ni(PyA\text{-}R)_3]^-$ and $[Ni(MeImA)_3]^-$ monoanions to generate such homo- and heterometallic complexes, which will allow us to study exchange-coupled interactions. Additionally, because the oxime N atom has been established to stabilize the valence states II+−IV+ of octahedral nickel,[14] we studied the synthesized compounds electrochemically. Moreover, involvement of the Ni^{III}/Ni^{II} couple has recently been reported[15] for the catalytic reaction of the novel nickel-containing superoxide dismutase (NiSOD), discovered in *streptomyces* soil bacteria and cyanobacteria. Of the redox-active nickel enzymes, only NiSOD[16] and NiFe hydrogenases[17] are capable of stabilizing the Ni^{3+} (low-spin, $S = {}^1/_2$) oxidation state in their active sites, although some catalytic cycles proposed for acetyl coenzyme A synthase (ACS)[18] have invoked transient intermediates with Ni^{3+} centers. We report here the synthesis, magnetic, electrochemical, spectroscopic, and other physical properties including the structures of the following compounds:

$$[Ni^{II}(PyA\text{-}H)_3Fe^{III}(PyA\text{-}H)_3Ni^{II}]ClO_4\ (\mathbf{1})$$

$$[LMn^{III}(PyA\text{-}H)_3Ni^{II}](ClO_4)_2\ (\mathbf{2})$$

$$[LNi^{II}(PyA\text{-}H)_3Ni^{II}]ClO_4\ (\mathbf{3a})$$

$$[LNi^{II}(PyA\text{-}Me)_3Ni^{II}]ClO_4\ (\mathbf{3b})$$

$$[LNi^{II}(PyA\text{-}Ph)_3Ni^{II}]ClO_4\ (\mathbf{3c})$$

$$[LNi^{II}(MeImA)_3Ni^{II}]ClO_4\ (\mathbf{4})$$

$$[LZn^{II}(PyA\text{-}H)_3Ni^{II}]ClO_4\ (\mathbf{5})$$

where PyA-R and MeImA represent the corresponding aldoximato anion and L a tridentate macrocyclic amine 1,4,7-trimethyl-1,4,7-triazacyclononane (Chart 1).

Additionally, to interpret the electrochemical results unambiguously, we prepared complex $[LZn^{II}(PyA\text{-}H)_3Zn^{II}]ClO_4$ (**6**), whose structural and electrochemical studies are also included. Moreover, in an earlier paper,[19] we have reported complexes, isostructural to **1**,

$$[Ni^{II}(PyA\text{-}H)_3Mn^{III}(PyA\text{-}H)_3Ni^{II}]ClO_4\ (\mathbf{7})$$

and

$$[Ni^{II}(PyA\text{-}H)_3Cr^{III}(PyA\text{-}H)_3Ni^{II}]ClO_4\ (\mathbf{8})$$

which will be on necessity mentioned here for comparison purposes. Throughout this paper, the compounds are denoted by the respective metal centers only, $Ni^{II}Fe^{III}Ni^{II}$ (**1**), $Mn^{III}Ni^{II}$ (**2**), $Ni^{II}Ni^{II}$ (**3a**−**c** and **4**), $Zn^{II}Ni^{II}$ (**5**), $Zn^{II}Zn^{II}$ (**6**), $Ni^{II}Mn^{III}Ni^{II}$ (**7**), and $Ni^{II}Cr^{III}Ni^{II}$ (**8**), for the sake of clarity.

Experimental Section

Materials and Physical Measurements. Reagent- or analytical-grade materials were obtained from commercial suppliers and used without further purification, except those for electrochemical measurements. Elemental analyses (C, H, N, and metal) were performed by the Microanalytical Laboratory, Mülheim, Germany.

---

(4) (a) Ross, S.; Weyhermüller, T.; Bill, E.; Bothe, E.; Flörke, U.; Wieghardt, K.; Chaudhuri, P. *Eur. J. Inorg. Chem.* **2004**, 984 and references cited therein. (b) Ross, S.; Weyhermüller, T.; Bill, E.; Wieghardt, K.; Chaudhuri, P. *Inorg. Chem.* **2001**, *40*, 6656.

(5) Burdinski, D.; Birkelbach, F.; Weyhermüller, T.; Flörke, U.; Haupt, H.-J.; Lengen, M.; Trautwein, A. X.; Bill, E.; Wieghardt, K.; Chaudhuri, P. *Inorg. Chem.* **1998**, *37*, 1009.

(6) Birkelbach, F.; Flörke, U.; Haupt, H.-J.; Butzlaff, C.; Trautwein, A. X.; Wieghardt, K.; Chaudhuri, P. *Inorg. Chem.* **1998**, *37*, 2000.

(7) Chaudhuri, P.; Rentschler, E.; Birkelbach, F.; Krebs, C.; Bill, E.; Weyhermüller, T.; Flörke, U. *Eur. J. Inorg. Chem.* **2003**, 541.

(8) Chaudhuri, P.; Winter, M.; Fleischhauer, P.; Haase, W.; Flörke, U.; Haupt, H.-J. *J. Chem. Soc., Chem. Commun.* **1990**, 1728.

(9) Chaudhuri, P.; Winter, M.; Della Védova, B. P. C.; Fleischhauer, P.; Haase, W.; Flörke, U.; Haupt, H.-J. *Inorg. Chem.* **1991**, *30*, 4777.

(10) Krebs, C.; Winter, M.; Weyhermüller, T.; Bill, E.; Wieghardt, K.; Chaudhuri, P. *J. Chem. Soc., Chem. Commun.* **1995**, 1913.

(11) Verani, C.; Weyhermüller, T.; Rentschler, E.; Bill, E.; Chaudhuri, P. *Chem. Commun.* **1998**, 2475.

(12) Verani, C.; Rentschler, E.; Weyhermüller, T.; Bill, E.; Chaudhuri, P. *J. Chem. Soc., Dalton Trans.* **2000**, 4263.

(13) Chaudhuri, P. *Coord. Chem. Rev.* **2003**, *243*, 143.

(14) (a) Chakravorty, A. *Isr. J. Chem.* **1985**, *25*, 99. (b) Lappin, A. G.; McAuley, A. *Adv. Inorg. Chem.* **1988**, *32*, 241. (c) Karmakar, S.; Choudhury, S. B.; Ganguly, S.; Chakravorty, A. *J. Chem. Soc., Dalton Trans.* **1997**, 585.

(15) (a) Wuerges, J.; Lee, J.-W.; Yim, Y.-I.; Yim, H.-S.; Kang, S.-O.; Carugo, K. D. *Proc. Natl. Acad. Sci. U.S.A.* **2004**, *101*, 8569. (b) Barondeau, D. P.; Kassmann, C. J.; Brun, C. K.; Tainer, J. A.; Getzoff, E. D. *Biochemistry* **2004**, *43*, 8038.

(16) Choudhury, S. B.; Lee, J. W.; Davidson, G.; Yim, Y. I.; Bose, K.; Sharma, M. L.; Kang, S. O.; Cabelli, D. E.; Maroney, M. J. *Biochemistry* **1999**, *38*, 3744.

(17) Davidson, G.; Choudhury, S. B.; Gu, Z. J.; Bose, K.; Roseboom, W.; Albracht, S. P. J.; Maroney, M. J. *Biochemistry* **2000**, *39*, 7468.

(18) Seravalli, J.; Kumar, M.; Ragsdale, S. W. *Biochemistry* **2002**, *41*, 1807.

(19) (a) Weyhermüller, T.; Wagner, R.; Khanra, S.; Chaudhuri, P. *Dalton Trans.* **2005**, 2539. (b) Birkelbach, F.; Weyhermüller, T.; Lengen, M.; Gerdan, M.; Trautwein, A. X.; Wieghardt, K.; Chaudhuri, P. *J. Chem. Soc., Dalton Trans.* **1997**, 4529.

Fourier transform IR spectra of the samples in KBr disks were recorded with a Perkin-Elmer 2000 FT-IR instrument. Electronic absorption spectra in solution were measured with a Perkin-Elmer Lambda 19 spectrophotometer. Magnetic susceptibilities of powdered samples were recorded with a SQUID magnetometer in the temperature range 2−290 K with an applied field of 1 T. Experimental susceptibility data were corrected for the underlying diamagnetism using Pascal's constants and for the temperature-independent paramagnetism contributions. Cyclic voltammetry (CV) and coulometric measurements were performed using EG&G equipment (potentiostat/galvanostat model 273A). Mass spectra were recorded with either a Finnigan MAT 8200 (electron ionization, EI-MS) or a MAT 95 (electrospray ionization, ESI-MS) instrument. A Bruker DRX 400 instrument was used for NMR spectroscopy. X-band electron paramagnetic resonance (EPR) spectra were recorded with a Bruker ELEXSYS E500 spectrometer equipped with a helium-flow cryostat (Oxford Instruments ESR 910).

Preparations. The macrocycle 1,4,7-trimethyl-1,4,7-triazacyclononane ($C_9H_{21}N_3$=L) was prepared as described previously.[20]

2-Acetylpyridinealdoxime [HPyA-Me]. To an ice-cold solution of Na_2CO_3 (1.06 g, 10 mmol) and $NH_2OH{\cdot}HCl$ (1.4 g, 20 mmol) in water (20 mL) was added 2-acetylpyridine (2.4 g, 20 mmol), and the resulting suspension was stirred at ∼4 °C for 2 h. The suspension was kept in a refrigerator overnight and then filtered to procure the solid material, which was washed with a cold methanol/water (1:3) solvent mixture. Yield: 2.4 g (∼88%). Purity checked by gas chromatography (GC): ∼98%. EI-MS: *m*/*z* 136 [M]$^+$.

1-Methyl-2-imidazolealdoxime [MeImAH]. A protocol very similar to that for HPyA-Me was used. Yield: 69%. Mp: 168−169 °C. Purity checked by GC: ∼99%. EI-MS: *m*/*z* 125 [M]$^+$.

[Ni^{II}(PyA-H)$_3$Fe^{III}(PyA-H)$_3$Ni^{II}]ClO$_4$ (1). To a light-green solution of $NiCl_2{\cdot}6H_2O$ (0.47 g, 2 mmol) in distilled methanol (50 mL) were added successively with stirring solid pyridine-2-aldoxime (HPyA-H; 0.72 g, 6 mmol) and $Fe(ClO_4)_2{\cdot}6H_2O$ (0.37 g, 1 mmol). To the resulting solution was added 10 mL of $[Bu_4N][OCH_3]$ (20% in CH_3OH), which upon stirring yielded a deep-brown solution. After 24 h, the precipitated brown microcrystalline substance was filtered, washed thoroughly with methanol, and air-dried. Yield: 0.51 g (∼51%). X-ray-quality black-brown crystals were obtained by diffusion of methanol to a dimethylformamide solution of **1.** Anal. Calcd for $C_{36}H_{30}ClFeNi_2N_{12}O_{10}$: C, 43.27; H, 3.03; N, 16.82; Ni, 11.75; Fe, 5.59. Found: C, 43.2; H, 3.0; N, 16.8; Ni, 11.9; Fe, 5.7. IR (KBr, cm^{-1}): 1663m, 1602s, 1541m, 1473s, 1431m, 1341m, 1220m, 1121s, 1080s, 1013m, 889m, 778m, 686s, 640s, 623m, 522m. ESI-MS (positive mode) in CH_3OH/H_2O: *m*/*z* (%) 899.0 (100%) [M − ClO$_4$]$^+$, 776.9 (20%) [M − ClO$_4$ − $C_6H_5N_2O$]$^+$.

[LMn^{III}(PyA-H)$_3$Ni^{II}](ClO$_4$)$_2$ (2). $Mn(ClO_4)_2{\cdot}6H_2O$ (0.36 g, 1 mmol) was added to a solution of 1,4,7-trimethyl-1,4,7-triazacyclononane (0.34 g, 2 mmol) in 25 mL of methanol under vigorous stirring, resulting in a brown solution. Another red-brown solution was produced by stirring $NiCl_2{\cdot}6H_2O$ (0.24 g, 1 mmol) and pyridinealdoxime (HPyA-H; 0.36 g, 3 mmol) in 25 mL of methanol. The above-mentioned two solutions were mixed together and stirred at room temperature for 15 min, to which sodium perchlorate monohydrate (0.14 g) dissolved in methanol (5 mL) was added. The solution yielded after 24 h red-brown needle-shaped crystals, which were filtered and dried in air. Yield: 0.38 g (∼45%). Parallelogram-shaped deep-brown crystals were grown from an acetonitrile solution for the X-ray structural characterization. Anal. Calcd for $C_{27}H_{36}Cl_2MnNiN_9O_{11}$ (847.18): C, 38.28; H, 4.28; N, 14.88; Mn, 6.48; Ni, 6.93. Found: C, 38.1; H, 4.3; N, 15.0; Mn, 6.6; Ni, 6.7. IR (KBr, cm^{-1}): 1604m, 1551w, 1537w, 1476m, 1465m, 1384w, 1345w, 1302w, 1218w, 1121s, 1091vs, 1054s, 1010m, 783m, 749w, 742w, 688w, 624m, 520w. UV−vis in CH_3CN [λ_{max}, nm (ϵ, M^{-1} cm^{-1})]: 248 (29 150) 310 (2959), 498sh (∼1578), 906 (34.7). ESI-MS (positive mode) in CH_2Cl_2: *m*/*z* (%) 764.1 (∼2) (MClO$_4^+$), 323.7 (∼1) (M^{2+}).

[LNi^{II}(PyA-H)$_3$Ni^{II}]ClO$_4$ (3a). To a solution of $NiCl_2{\cdot}6H_2O$ (0.48 g, 2 mmol) in 25 mL of distilled methanol was added with stirring 1,4,7-trimethyl-1,4,7-triazacyclononane (0.17 g, 1 mmol). To the resulting greenish-blue solution were added pyridine-2-aldoxime (HPyA-H; 0.36 g, 3 mmol) and triethylamine (1 mL). The solution was stirred for 0.5 h to yield a dark-brown solution, which was kept open overnight for evaporation. The solid was taken up in acetonitrile, and the mixture was filtered to remove any solid particles. The acetonitrile solution yielded after 1 week deep-brown crystals, which were collected by filtration. Yield: 0.25 g (33%). Deep-brown crystals were grown from an acetonitrile solution for the X-ray structural characterization. Anal. Calcd for $C_{27}H_{36}ClNi_2N_9O_7$: C, 43.15; H, 4.83; N, 16.78; Ni, 15.62. Found: C, 43.1; H, 4.8; N, 16.6; Ni, 15.6. IR (KBr, cm^{-1}): 1601s, 1530m, 1474s, 1159m, 1138s, 1120s, 1096s, 1014m, 989m, 779m, 680m, 624m. UV−vis in CH_2Cl_2 [λ_{max}, nm (ϵ, M^{-1} cm^{-1})]: 276 (38 965), 336 (27 280), 498 (569), 827 (31), 949 (41^). ESI-MS (positive mode) in CH_3OH: *m*/*z* (%) 650.3 (100%) [M − ClO$_4$]$^+$.

[LNi^{II}(PyA-Me)$_3$Ni^{II}]ClO$_4$ (3b) and [LNi^{II}(PyA-Ph)$_3$Ni^{II}]ClO$_4$ (3c). Complexes **3b** and **3c** were prepared by the same protocol as that for **3a** using HPyA-Me for **3b** and HPyA-Ph for **3c**. Deep-brown crystals were grown from a methanol solution for the X-ray structural characterization. Complex **3b**. Yield: 0.30 g (37%). Anal. Calcd for $C_{30}H_{42}ClN_9Ni_2O_7$: C, 45.41; H, 5.34; N, 15.89; Ni, 14.79. Found: C, 45.6; H, 5.4; N, 15.9; Ni, 14.8. IR (KBr, cm^{-1}): 3007, 2961, 2893, 2856, 2816m, 1594s, 1571m, 1524s, 1463s, 1203s, 1188s, 1180s, 1107s, 1086s, 1045m, 1018m, 990m, 780s, 750m, 700m, 638m, 622m. UV−vis in CH_2Cl_2 [λ_{max}, nm (ϵ, M^{-1} cm^{-1})]: 285 (31 500), 341 (22 660), 483 (540). ESI-MS (positive mode) in CH_3OH: *m*/*z* (%) 692.3 (100%) [M − ClO$_4$]$^+$. Complex **3c**. Yield: 0.69 g (70%). Anal. Calcd for $C_{45}H_{48}ClN_9Ni_2O_7$: C, 55.17; H, 4.94; N, 12.87; Ni, 11.98. Found: C, 55.2; H, 5.0; N, 12.8; Ni, 12.0. IR (KBr, cm^{-1}): 2886m, 2816m, 1590s, 1568m, 1456s, 1440s, 1263m, 1218s, 1142s, 1123s, 1107s, 1060s, 1017s, 975s, 792m, 780s, 745m, 708s, 638m, 622m. UV−vis in CH_2Cl_2 [λ_{max}, nm (ϵ, M^{-1} cm^{-1})]: 291 (31 500), 349 (19 300), 510 (580), 833 (35), 942 (40). ESI-MS (positive mode) in CH_3OH: *m*/*z* (%) 880.3 (100%) [M − ClO$_4$]$^+$.

[LNi^{II}(MeImA)$_3$Ni^{II}]ClO$_4$ (4). The same protocol as that for **3a** was used for preparing complex **4** by replacing pyridine-2-aldoxime with 1-methylimidazole-2-aldoxime. Deep-brown crystals were obtained from a methanol solution for the X-ray structure determination. Yield: 0.59 g (77%). Anal. Calcd for $C_{24}H_{39}ClN_{12}Ni_2O_7$: C, 37.91; H, 5.17; N, 22.10; Ni, 15.43. Found: C, 38.0; H, 5.2; N, 22.0; Ni, 15.1. IR (KBr, cm^{-1}): 3552m, 3408m, 3237m, 3113m, 2890m, 2854m, 2813m, 1557s, 1458s, 1293m, 1282m, 1220s, 1137s, 1106s, 1057s, 1013s, 865m, 776m, 746m, 717m, 672m, 624m. UV−vis in CH_2Cl_2 [λ_{max}, nm (ϵ, M^{-1} cm^{-1})]: 442 (340), 648 (30), 820 (30), 955 (44). ESI-MS (positive mode) in CH_3OH: *m*/*z* (%) 659.3 (100%) [M − ClO$_4$]$^+$.

[LZn^{II}(PyA)$_3$Ni^{II}]ClO$_4$ (5). Zinc chloride (0.136 g, 1 mmol) was added to a solution of 1,4,7-trimethyl-1,4,7-triazacyclononane (0.17 g, 1 mmol) in 25 mL of methanol under vigorous stirring, resulting in a pale-yellow solution. Another orange-red solution was produced by stirring $Ni(ClO_4)_2{\cdot}6H_2O$ (0.37 g, 1 mmol), pyridine-2-aldoxime

---

(20) Wieghardt, K.; Chaudhuri, P.; Nuber, B.; Weiss, J. *Inorg. Chem.* **1982**, *21*, 3086.

(0.36 g, 3 mmol), and 0.7 mL of Et_3N in 25 mL of methanol. The above-mentioned two solutions were mixed together and stirred at room temperature for 0.5 h, whereupon an orange solid precipitated out. The solid was separated by filtration and crystallized from an acetonitrile solution to yield X-ray-quality red-brown crystals of **4**·H_2O. Yield: 0.47 g (62%). Anal. Calcd for $C_{27}H_{36}ClN_9NiO_7Zn$: C, 42.77; H, 4.79; N, 16.63; Zn, 8.62; Ni, 7.74. Found: C, 42.8; H, 4.7; N, 16.6; Zn, 8.8; Ni, 7.7. IR (KBr, cm^{-1}): 1602s, 1533m, 1519m, 1475s, 1463m, 1230w, 1158m, 1131s, 1116s, 1091s, 1018m, 988m, 780m, 680m, 624m. UV−vis in CH_2Cl_2 [λ_{max}, nm (ϵ, M^{-1} cm^{-1})]: 425sh (∼21), 500sh (∼149), 774 (17.2). ESI-MS (positive mode) in CH_2Cl_2: *m/z* (%) 656.2 (100%) $[M - ClO_4]^+$.

$[LZn^{II}(PyA)_3Zn^{II}]ClO_4$ (6). To a solution of 1,4,7-trimethyl-1,4,7-triazacyclononane (0.17 g, 1 mmol), pyridine-2-aldoxime (0.36 g, 3 mmol), and Et_3N (1 mL) in methanol (50 mL) was added with stirring zinc acetate dihydrate (0.44 g, 2 mmol) to provide a pale-yellow solution. The solution kept overnight under a hood yielded a very pale-yellow microcrystalline solid of **5**, which was recrystallized from methanol. Yield: 0.5 g (∼65%). Anal. Calcd for $C_{27}H_{36}ClN_9O_7Zn_2$: C, 42.40; H, 4.74; N, 16.48; Zn, 17.10. Found: C, 42.3; H, 4.8; N, 16.5; Zn, 17.2. IR (KBr, cm^{-1}): 3607m, 3383br, 1647m, 1603s, 1583m, 1541s, 1481s, 1462s, 1434m, 1342m, 1299m, 1227m, 1155m, 1085s, 1017s, 989m, 892m, 781m, 686m, 624m. UV−vis in CH_3CN [λ_{max}, nm (ϵ, M^{-1} cm^{-1})]: 272 (2.38×10^4), 321 (1.78×10^4). ESI-MS (positive) in CH_2Cl_2: *m/z* (%) 664 (100%) $[M - ClO_4]^+$.

***Caution!** Although we experienced no difficulties with the compounds isolated as their perchlorate salts, the unpredictable behavior of perchlorate salts necessitates extreme caution in their handling.*

X-ray Crystallographic Data Collection and Refinement of the Structures. The crystallographic data for **1**−**6** are summarized in Table 1. Graphite-monochromated Mo Kα radiation (λ = 0.710 73 Å) was used for **1**−**5**, whereas a copper source (λ = 1.541 78 Å) was used for **6**. Dark-red/brown to light-red crystals of **1**−**5** or pale-yellow crystals of **6** were fixed with perfluoropolyether onto glass fibers and mounted on a Bruker Kappa CCD for **1**−**5** or a Siemens SMART diffractometer for **6** equipped with a cryogenic nitrogen cold stream, and intensity data were collected at 100(2) K. Final cell constants were obtained from a least-squares fit of all measured reflections. Intensity data were corrected for Lorentz and polarization effects. The data sets were not corrected for absorption, except for **4** and **6**, for which the program *SADABS* (version 2.1) was used for absorption corrections. The Siemens *ShelXTL* software package (Sheldrick, G. M. Universität Göttingen, Göttingen, Germany) was used for solution, refinement, and artwork of the structures; the neutral atom scattering factors of the program were used.

Results and Discussion

The thermodynamic stability of the in situ generated $[Ni(PyA-R)_3]^-$ monoanion containing three facially disposed pendent oxime O atoms for ligation, together with the lability of the first transition series divalent metal ions, is utilized to synthesize homo- and heterometallic complexes. Although no scrambling was observed, all attempts to strictly synthesize the cation $[LNi^{II}(PyA-H)_3Zn^{II}]^+$, a constitution isomer of complex **5**, failed. On the other hand, complex **5** $[LZn^{II}(PyA-H)_3Ni^{II}]^+$ was readily isolated starting from its respective materials. This can be attributed to the greater thermodynamic stability of the $[Ni(PyA-H)_3]^-$ anion than that of the $[LNi(solvent)_3]^{2+}$ cation. In other words, the $[Zn(PyA-H)_3]^-$ monoanion is less stable than the $[Ni(PyA-H)_3]^-$ ion. The color of complexes **1**−**5** is light to deep red-brown and is dominated by the $Ni^{II}(N_{py})_3(N_{azomethine})_3$ chromophore. They are completely air-stable in the solid state and also in solution for a few days.

Because the relevant bands in the IR spectra of comparable pyridine-2-aldoximate-containing heteronuclear $Cr^{III}M^{II}$ and $Fe^{III}M^{II}$ complexes have been reported earlier by us[4] and the spectra of complexes **1**−**6**, except for **4**, are also very similar, we refrain from discussing them again. The bands are given in the Experimental Section.

The electronic spectral results indicate that complexes **2**−**5** are stable in solution. On the basis of their high extinction coefficients and transitions similar to those reported in the literature[21] and a comparison with the spectrum of only a Zn^{II}-containing complex, **6** (see the Experimental Section), all bands below 350 nm for complexes are assigned to $\pi-\pi^*$ transitions of the oxime ligand. Judged on the basis of their low extinction coefficients, we tentatively ascribe the bands at 906 nm for **2**, 498, 827, and 949 nm for **3a**, 483 nm for **3b**, 510, 833, and 942 nm for **3c**, 442, 648, 820, and 955 nm for **4**, and 774 nm for **5** to d−d transitions at the Ni^{II} centers.

ESI-MS in the positive ion mode has been proven to be a very useful analytical tool, except for **2**, for characterizing all complexes (see the Experimental Section), which show the monopositively charged species $[M - ClO_4]^+$ as the base peak (100%). The Mn-containing complex **2** does not provide signals for unambiguous characterization, which is in accordance with our own earlier experience.[19]

Description of the Structures. The crystal structures of complexes **1**−**6** have been determined by single-crystal X-ray crystallography at 100(2) K. The X-ray structures confirm that tri- and dinuclear complexes, $Ni^{II}Fe^{III}Ni^{II}$ (**1**), $Mn^{III}Ni^{II}$ (**2**), $Ni^{II}Ni^{II}$ (**3a**−**c** and **4**), $Zn^{II}Ni^{II}$ (**5**), and $Zn^{II}Zn^{II}$ (**6**), have indeed been formed in which two (for **2**−**6**) or three (for **1**) pseudooctahedral polyhedra are joined face-to-face by three oximato N−O groups. The N_{ox}−O bond lengths of average = 1.347 ± 0.004 (**1**), 1.358 ± 0.01 (**2**), 1.331 ± 0.006 (**3** and **4**), 1.341 ± 0.007 (**5**), and 1.341 ± 0.004 Å (**6**) are nearly identical with those for other comparable structures[4,9,19,22] and significantly shorter than ∼1.40 Å in general for free oxime ligands. The bond angle $C{=}N_{ox}{-}O$ [average 117.7 ± 0.3° (**1**), 117.8 ± 0.8° (**2**), 119.3 ± 0.3° (**3** and **4**), 118.7 ± 0.4° (**5**), and 118.5 ± 0.3° (**6**)] and the bond distance $C{=}N_{ox}$ [average 1.296 ± 0.006 (**1**), 1.286 ± 0.004 (**2**), 1.298 ± 0.005 (**3** and **4**), 1.288 ± 0.006 Å (**5**), and 1.287 ± 0.005 Å (**6**)] are, as expected, identical with those for other $Fe^{III}M^{II}$,

---

(21) Burger, K.; Ruff, I.; Ruff, F. *J. Inorg. Nucl. Chem.* **1965**, *27*, 179.

(22) (a) Beckett, R.; Hoskins, B. F. *J. Chem. Soc., Dalton Trans.* **1972**, *291*, 2527. (b) Nasakkala, M.; Saarinen, H.; Korvenranta, J.; Orama, M. *Acta Crystallogr., Sect. C* **1989**, *45*, 1511. (c) Pearse, G. A.; Raithby, P.; Lewis, J. *Polyhedron* **1989**, *8*, 301. (d) Schlemper, E. O.; Stunkel, J.; Patterson, C. *Acta Crystallogr., Sect. C* **1990**, *46*, 1226. (e) Nordquest, K. W.; Phelps, D. W.; Little, W. F.; Hodgson, D. J. *J. Am. Chem. Soc.* **1976**, *98*, 1104. (f) Churchill, M. R.; Reis, A. H. *Inorg. Chem.* **1972**, *11*, 1811. (g) Churchill, M. R.; Reis, R. H. *Inorg. Chem.* **1972**, *11*, 2299. (h) Faller, J. W.; Blankenship, C.; Whitmore, B.; Sena, S. *Inorg. Chem.* **1985**, *24*, 4483. (i) Churchill, M. R.; Reis, A. H. *Inorg. Chem.* **1973**, *12*, 2280.

Table 1. Crystallographic Data for **1**, **2**$\cdot CH_3CN$, **3a**$\cdot H_2O$, **3b**$\cdot 0.5CH_3OH$, **3c**, **4**$\cdot 1.5H_2O$, **5**, and **6**$\cdot 3CH_3OH\cdot 3H_2O$

	$Ni^{II}Fe^{III}Ni^{II}$ (**1**)	$Mn^{III}Ni^{II}$ (**2**)	$Ni^{II}Ni^{II}$(PyA-H) (**3a**)	$Ni^{II}Ni^{II}$(PyA-Me) (**3b**)
empirical formula	$C_{36}H_{30}ClFeN_{12}Ni_2O_{10}$	$C_{29}H_{39}Cl_2MnN_{10}NiO_{11}$	$C_{27}H_{38}ClN_9Ni_2O_8$	$C_{30.5}H_{44}ClN_9Ni_2O_{7.5}$
fw	999.44	888.25	769.53	809.62
T, K	100(2)	100(2)	100(2)	100(2)
wavelength, Å	0.710 73	0.710 73	0.710 73	0.710 73
cryst syst, space group	trigonal, $R\bar{3}$	monoclinic, $C2/c$	monoclinic, $P2_1$	triclinic, $P\bar{1}$
unit cell dimens				
a, Å	13.835(2)	19.9574(7)	9.2784(3)	11.6289(4)
b, Å	13.835(2)	24.6226(9)	16.5598(9)	13.8230(5)
c, Å	21.163(4)	14.9959(6)	11.3633(6)	13.8607(5)
α, deg	90	90	90	119.548(3)
β, deg	90	90.73(1)	112.61(1)	101.498(3)
γ, deg	120	90	90	102.176(3)
V, Å^3; Z	3508.1(10); 3	7368.4(5); 8	1611.76(13); 2	1770.03(11); 2
calcd density, Mg/m^3	1.419	1.601	1.586	1.519
abs coeff, mm^{-1}	1.223	1.070	1.314	1.200
F(000)	1527	3664	800	846
cryst size, mm	0.09 × 0.08 × 0.06	0.04 × 0.03 × 0.02	0.10 × 0.04 × 0.03	0.30 × 0.26 × 0.18
abs corrn	not corrected	not corrected	not corrected	not corrected
refinement method	full-matrix least squares on F^2	full-matrix least squares on F^2	full-matrix least squares on F^2	full-matrix least squares on F^2
data/restraints/param	1875/19/112	11 701/0/507	10 193/2/433	10 284/0/462
GOF on F^2	1.122	1.025	1.053	1.044
final *R* indices [$I > 2\sigma(I)$]	R1 = 0.0626, wR2 = 0.1785	R1 = 0.0500, wR2 = 0.0983	R1 = 0.0484, wR2 = 0.0761	R1 = 0.0289, wR2 = 0.0708
R indices (all data)	R1 = 0.0920, wR2 = 0.2041	R1 = 0.0860, wR2 = 0.1130	R1 = 0.0673, wR2 = 0.0820	R1 = 0.0314, wR2 = 0.0722
largest diff peak and hole, e A^{-3}	0.915 and −0.384	1.068 and −0.935	0.627 and −0.482	0.623 and −0.497
absolute structure param			−0.001(9)	

	$Ni^{II}Ni^{II}$(PyA-Ph) (**3c**)	$Ni^{II}Ni^{II}$(MeImA) (**4**)	$Zn^{II}Ni^{II}$ (**5**)	$Zn^{II}Zn^{II}$ (**6**)
empirical formula	$C_{45}H_{48}ClN_9Ni_2O_7$	$C_{24}H_{42}ClN_{12}Ni_2O_{8.5}$	$C_{27}H_{38}ClN_9NiO_8Zn$	$C_{30}H_{54}ClN_9O_{13}Zn_2$
fw	979.79	787.57	776.19	915.01
T, K	100(2)	100(2)	100(2)	100(2)
wavelength, Å	0.710 73	0.710 73	0.710 73	1.541 78
cryst syst, space group	cubic, $Pa\bar{3}$	monoclinic, $C2/c$	monoclinic, $P2_1$	trigonal, $R3c$
unit cell dimens				
a, Å	20.9553(3)	17.8083(4)	9.3049(3)	11.9820(4)
b, Å	20.9553(3)	15.7015(4)	16.6595(6)	11.9820(4)
c, Å	20.9553(3)	24.5793(6)	11.3975(4)	47.0659(13)
α, deg	90	90	90	90
β, deg	90	104.911(4)	112.472(5)	90
γ, deg	90	90	90	120
V, Å^3; Z	9202.0(2); 8	6641.4(3); 8	1632.62(10); 2	5581.9(3); 6
calcd density, Mg/m^3	1.414	1.575	1.579	1.558
abs coeff, mm^{-1}	0.936	1.281	1.455	2.775
F(000)	4080	3288	804	2868
cryst size, mm	0.20 × 0.15 × 0.14	0.30 × 0.20 × 0.16	0.08 × 0.05 × 0.04	0.22 × 0.22 × 0.14
abs corrn	not corrected	semiempirical from equivalents	not corrected	SADABS V2.1, Bruker-Nonius
refinement method	full-matrix least squares on F^2	full-matrix least squares on F^2	full-matrix least squares on F^2	full-matrix least squares on F^2
data/restraints/param	5551/14/216	11 969/13/460	10 363/2/433	2395/4/174
GOF on F^2	1.166	1.112	1.022	1.076
final *R* indices [$I > 2\sigma(I)$]	R1 = 0.0464, wR2 = 0.1186	R1 = 0.0414, wR2 = 0.0991	R1 = 0.0254, wR2 = 0.0567	R1 = 0.0523, wR2 = 0.1401
R indices (all data)	R1 = 0.0521, wR2 = 0.1218	R1 = 0.0468, wR2 = 0.1018	R1 = 0.0287, wR2 = 0.0581	R1 = 0.0526, wR2 = 0.1406
largest diff peak and hole, e A^{-3}	1.426 and −0.500	0.887 and −0.741	0.481 and −0.291	0.960 and −1.310
absolute structure param			−0.001(5)	0.07(5)

$Mn^{III}M^{II}$, and $Cr^{III}M^{II}$ complexes containing pyridine-2-aldoximato reported earlier by us.[4,13]

X-ray Structure of 1. The lattice consists of discrete trinuclear monocations and perchlorate anions. The heterotrinuclear complex, $Ni^{II}Fe^{III}Ni^{II}$ (**1**), crystallizes in the space group $R\bar{3}$, with threefold inversion symmetry and, as expected, is isostructural with the analogous $Ni^{II}Mn^{III}Ni^{II}$ (**7**) and $Ni^{II}Cr^{III}Ni^{II}$ (**8**) complexes, described earlier by us.[19a] The trinuclear complex contains two $Ni^{II}(PyA)_3^-$ moieties, each having a NiN_6 coordination sphere, acting as a tridentate ligand through the pendent oximato O atoms to the centrally placed Fe^{III} ion. A view of the cation $[Fe(PyA\text{-}H)_6Ni_2]^+$ in complex **1** is shown in Figure 1. Selected bond distances and angles are listed in Table 2. The cation $[Fe(PyA\text{-}H)_6Ni_2]^+$ having a crystallographic threefold inversion symmetry has therefore a strictly linear arrangement of the $Ni^{II}Fe^{III}Ni^{II}$ array, and the two $Ni(PyA)_3^-$ units necessarily have opposite chirality (Δ and Λ), making $[Fe(PyA\text{-}H)_6Ni_2]^+$ achiral.

The terminal Ni centers are sixfold-coordinated, yielding a NiN_6 core; coordination occurs facially through three

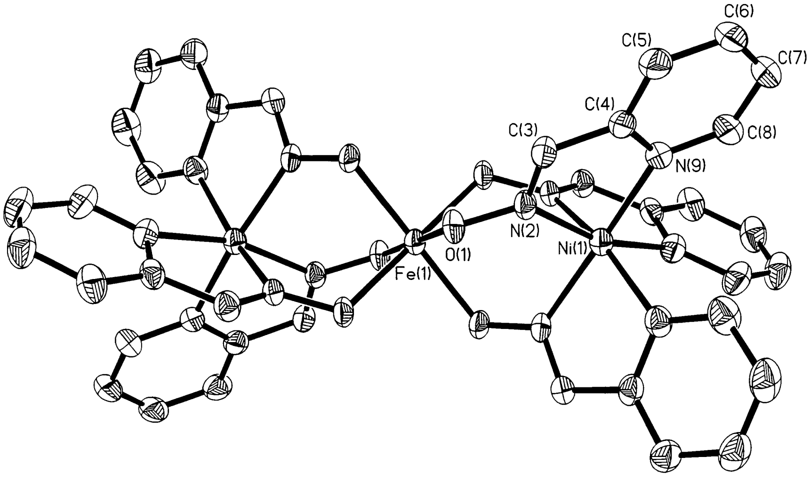

Figure 1. ORTEP diagram of the cation in $Ni^{II}Fe^{III}Ni^{II}$ (**1**) with 50% probability of the ellipsoids.

Table 2. Selected Bond Lengths (Å) and Angles (deg) for Complex **1**[a]

Ni(1)−N(2)	2.001(3)	C(3)−N(2)	1.296(6)
Ni(1)−N(9)	2.075(4)	N(2)−O(1)	1.347(4)
Fe(1)−O(1)	2.019(3)		
N(2)−Ni(1)−N(2)#2	89.14(14)	N(9)#2−Ni(1)−N(9)	92.92(14)
N(2)−Ni(1)−N(9)#2	101.68(14)	N(2)#3−Ni(1)−N(9)#3	78.54(14)
N(2)−Ni(1)−N(9)	78.55(14)	N(9)#2−Ni(1)−N(9)#3	92.91(14)
N(2)#2−Ni(1)−N(9)	163.37(15)		
N(9)−Ni(1)−N(9)#3	92.91(14)	C(3)−N(2)−O(1)	117.7(3)
O(1)#1−Fe(1)−O(1)	180.0	C(3)−N(2)−Ni(1)	117.9(3)
N(2)−O(1)−Fe(1)	115.8(2)	O(1)−N(2)−Ni(1)	124.3(3)
Ni···Fe	3.545		

[a] Symmetry transformations used to generate equivalent atoms: #1, $-x + {}^{2}/_{3}, -y + {}^{4}/_{3}, -z + {}^{1}/_{3}$; #2, $-x + y, -x + 1, z$; #3, $-y + 1, x - y + 1, z$; #4, $x - y + {}^{2}/_{3}, x + {}^{1}/_{3}, -z + {}^{1}/_{3}$; #5, $y - {}^{1}/_{3}; -x + y + {}^{1}/_{3}, -z + {}^{1}/_{3}$; #6, $y - {}^{1}/_{3}, -x + y + {}^{1}/_{3}, -z - {}^{2}/_{3}$; #7, $x - y + {}^{2}/_{3}, x + {}^{1}/_{3}, -z - {}^{2}/_{3}$.

pyridine $N_{py}(9)$ atoms and three azomethine $N_{ox}(2)$ atoms, from the pyridine-2-aldoximate ligands (Figure 1). The Ni(1)−N_{ox}(2) bond length = 2.001(3) Å is shorter than the Ni(1)−N_{py}(9) = 2.075(4) Å bond distance, as has been observed earlier for comparable complexes.[4,19a] The Ni−N bond lengths fall within the ranges that are considered as normal covalent bonds for high-spin d^8 Ni^{II} ions. The facial disposition of the three $N_{py}N_{ox}$ chelate rings at each Ni atom is necessary for the ligation of the pendent oxime O atoms, O(1) and its equivalents, to the central iron. The chelate rings are planar. The average chelate bite angle on the two Ni centers is 86.9°. This small but significant negative deviation of the bite angle from 90° necessarily implies the presence of substantial trigonal distortion. Indeed, the two Ni centers can be considered to have distorted trigonal-antiprismatic coordination, as is evident from the average twist angle ψ of 40.0°, which deviates appreciably from the ideal 60° for an octahedron. The trigonal twist angle ψ is defined as the angle between the triangular faces comprising three pyridine N atoms, N(9) and its equivalents, and three azomethine N atoms, N(2) and its equivalents. That the array Ni(N−O)Fe is not planar is shown by the dihedral angle θ of 38.4° between the planes comprising Fe(O−N) and Ni(N−O) atoms. These distortions of the six-coordinate d^8 Ni^{II} ion in complex **1** can be ascribed to both electronic (LFSE) and size effects, as has been discussed earlier.[5,23]

The central iron atom Fe(1) is surrounded by an almost perfect octahedron (with the deviation being less than 4°) of six oximato oxygen atoms O(1), pendant from the two $Ni(PyA\text{-}H)_3^-$ fragments. All angles at the metal between cis O atoms deviate from ideal 90°, being 86.78(11)° and 93.22(11)°; the *cis*-Fe(1)−O bond angle of 93.22(11)° represents the O atoms originating from the same $Ni(PyA\text{-}H)_3^-$ fragment, whereas the angle 86.78(11)° is exhibited between the O atoms of two different $Ni(PyA\text{-}H)_3^-$ fragments. The Fe(1)−O(1) distance of 2.019(3) Å compares favorably with that [2.021(7) Å] in a very similar oximato-bridged trinuclear Fe^{II}(low-spin)Fe^{III}(high-spin)Fe^{II}(low-spin)[24] as well as with those in other $Fe^{III}O_6$ species.[25,26] That the central Fe(1) ion should be ascribed to a III+ (d^5 high-spin) oxidation level is borne out additionally by the facts that (i) a perchlorate anion is present for maintaining the electroneutrality of the monocationic $[Fe(PyA\text{-}H)_6Ni_2]^+$ complex and (ii) the magnetic data can only be simulated by considering an $S_{Fe} = {}^{5}/_{2}$ for the central Fe(1) center. We conclude that complex **1** contains a $Ni^{II}_2Fe^{III}$ (high-spin) core. Mössbauer data at 80 K and zero field also support the high-spin formulation of the ferric center ($\delta_{Fe} = 0.57$ mm·s^{-1}; $\Delta E_Q = -0.05$ mm·s^{-1}).

Molecular Structure of 2·CH_3CN. The structure of **2**, shown in Figure 2, clearly illustrates the heterodinuclear nature of the complex. Selected bond lengths and angles for complex **2** are given in Table 3. A $[Ni(PyA\text{-}H)_3]^-$ anion coordinates to a Mn^{III} center through its deprotonated oxime O atoms with a Mn···Ni separation of 3.506 Å. The Mn

---

(23) (a) Wentworth, R. A. D. *Coord. Chem. Rev.* **1972/73**, *9*, 171. (b) Kirchner, R. M.; Meali, C.; Bailey, M.; Howe, N.; Torne, L. P.; Wilson, L. J.; Andrews, L. C.; Rose, N. J.; Lingafelter, E. C. *Coord. Chem. Rev.* **1987**, *77*, 89. (c) Kunow, S. A.; Takeuchi, K. J.; Grzybowski, J. J.; Jircitano, A. J.; Goedken, V. L. *Inorg. Chim. Acta* **1996**, *241*, 21.

(24) Pal, S.; Melton, T.; Mukherjee, R.; Chakravorty, A. R.; Tomas, M.; Falvello, L. R.; Chakravorty, A. *Inorg. Chem.* **1985**, *24*, 1250.

(25) *Comprehensive Coordination Chemistry*; Wilkinson, G., Ed.; Pergamon: England, 1987; Vol. 4.

(26) (a) Beattle, J. K.; Best, S. P.; Skelton, W. W.; White, A. H. *J. Chem. Soc., Dalton Trans.* **1981**, 2105. (b) Hair, N. J.; Beattle, J. K. *Inorg. Chem.* **1977**, *16*, 245. (c) Linder, Von H. J.; Gottlicher, S. *Acta Crystallogr., Sect. B: Struct. Crystallogr. Cryst. Chem.* **1969**, *B25*, 832. (d) Iball, J.; Morgan, C. H. *Acta Crystallogr.* **1967**, *23*, 239.

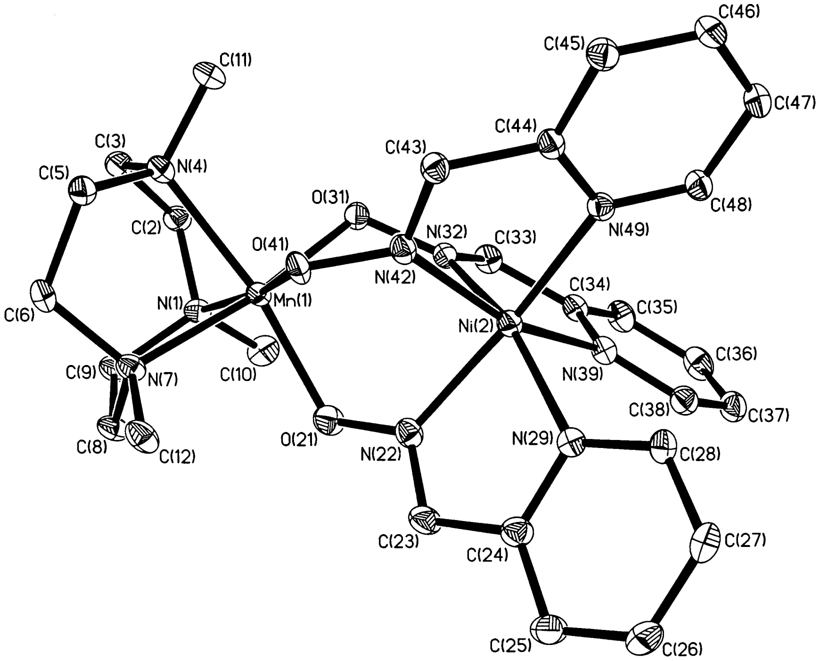

Figure 2. Molecular structure of the cation in complex $Mn^{III}Ni^{II}$ (**2**).

Table 3. Selected Bond Lengths (Å) and Angles (deg) for Complex **2**·CH_3CN^a

Mn(1)−O(31)	1.932(2)	Ni(2)−N(22)	2.043(3)
Mn(1)−O(21)	1.996(3)	Ni(2)−N(32)	2.050(2)
Mn(1)−O(41)	2.029(2)	Ni(2)−N(42)	2.058(3)
Mn(1)−N(7)	2.106(3)	Ni(2)−N(49)	2.094(2)
Mn(1)−N(4)	2.168(3)	Ni(2)−N(29)	2.100(2)
Mn(1)−N(1)	2.195(3)	Ni(2)−N(39)	2.108(3)
O(21)−N(22)	1.346(3)	N(32)−C(33)	1.278(4)
N(22)−C(23)	1.287(4)	O(41)−N(42)	1.346(3)
O(31)−N(32)	1.359(3)	N(42)−C(43)	1.286(4)
O(31)−Mn(1)−O(21)	98.67(10)	N(22)−Ni(2)−N(32)	87.25(10)
O(31)−Mn(1)−O(41)	95.08(9)	N(22)−Ni(2)−N(42)	88.61(11)
O(21)−Mn(1)−O(41)	96.70(9)	N(32)−Ni(2)−N(42)	86.68(10)
O(31)−Mn(1)−N(7)	169.32(10)	N(22)−Ni(2)−N(49)	163.11(10)
O(21)−Mn(1)−N(7)	89.34(11)	N(32)−Ni(2)−N(49)	102.15(10)
O(41)−Mn(1)−N(7)	90.96(9)	N(42)−Ni(2)−N(49)	78.09(10)
O(31)−Mn(1)−N(4)	88.75(10)	N(22)−Ni(2)−N(29)	78.27(10)
O(21)−Mn(1)−N(4)	167.97(10)	N(32)−Ni(2)−N(29)	161.48(10)
O(41)−Mn(1)−N(4)	92.03(10)	N(42)−Ni(2)−N(29)	104.25(10)
N(7)−Mn(1)−N(4)	82.23(11)	N(49)−Ni(2)−N(29)	94.81(10)
O(31)−Mn(1)−N(1)	91.32(10)	N(22)−Ni(2)−N(39)	101.63(11)
O(21)−Mn(1)−N(1)	89.47(10)	N(32)−Ni(2)−N(39)	77.89(11)
O(41)−Mn(1)−N(1)	170.34(10)	N(42)−Ni(2)−N(39)	160.93(10)
N(7)−Mn(1)−N(1)	81.66(10)	N(49)−Ni(2)−N(39)	94.12(10)
N(4)−Mn(1)−N(1)	80.85(11)	N(29)−Ni(2)−N(39)	93.65(11)
N(22)−O(21)−Mn(1)	113.2(2)	C(33)−N(32)−Ni(2)	117.3(2)
C(23)−N(22)−O(21)	118.3(3)	O(31)−N(32)−Ni(2)	125.3(2)
C(23)−N(22)−Ni(2)	116.9(2)	N(42)−O(41)−Mn(1)	112.6(2)
O(21)−N(22)−Ni(2)	124.6(2)	C(43)−N(42)−O(41)	118.1(3)
N(32)−O(31)−Mn(1)	111.7(2)	C(43)−N(42)−Ni(2)	116.9(2)
C(33)−N(32)−O(31)	117.2(3)	O(41)−N(42)−Ni(2)	124.6(2)
Mn(1)···Ni(2)	3.506		

[a] Symmetry transformations used to generate equivalent atoms: #1, $-x + 1, y, -z + {}^1/_2$; #2, $-x + 1, y, -z + {}^3/_2$.

coordination geometry is distorted octahedral with three N atoms from the facially coordinated tridentate amine and three O atoms from three oximate groups. The observed Mn(1)−O and Mn(1)−N bond distances (Table 3) are in agreement with those reported for high-spin Mn^{III} centers with the macrocyclic amine;[6,25,27] the N(1)−Mn(1)−O(41) axis defines an elongated Jahn−Teller axis of a high-spin d^4 ion in a distorted octahedral ligand field.

The Ni center, Ni(2), in **2** is also sixfold-coordinated, yielding a NiN_6 core. Coordination occurs facially through pyridine N atoms, N(29), N(39), and N(49), and three azomethine N atoms, N(22), N(32), and N(42) from a pyridine-2-aldoxime (PyA-H) ligand. The average $Ni-N_{py} = 2.113 \pm 0.009$ Å and average $Ni-N_{ox} = 2.030 \pm 0.01$ Å are nearly identical with those observed for **1**, **3a**−**c**, **4**, **5**, and similar comparable structures.[4,19a] The Ni^{II} center is trigonally distorted with an average twist angle of 39.3°. Like complex **1**, the tris(pyridine-2-aldoximato)nickel(II) unit in **2** is identical with those reported earlier by us,[4] and hence we will refrain from describing it again. In summary, the crystal structure of **2** unequivocally establishes the presence of the $Mn^{III}Ni^{II}$ core in the cation of $[LMn(PyA\text{-}H)_3Ni](ClO_4)_2$.

Molecular Structures of 3a·H_2O, 3b·0.5H_2O, 3c·1.5H_2O, 4, and 5. Because the structures of **3a**−**c** and **4** are very similar with respect to the atom connectivity and the geometry of the Ni centers, we confine our structure description to that of **3a**; the crystal data for all four compounds are listed in Table 1.

The structure of **3a** consists of one distinct $[LNi_2(PyA\text{-}H)_3]^+$ cation, one noncoordinatively bound perchlorate anion, and one molecule of water of crystallization. A perspective view of the cation in **3a** is shown in Figure 3. Table 4 lists selected bond distances and angles for complex **3a**. Both Ni centers, Ni(1) and Ni(2), are in a distorted octahedral geometry with the core structure $N_3Ni(1)(O-N_{ox})_3Ni(2)(N_{py})_3$. The three atoms N(1), N(4), and N(7) of the facially coordinated tridentate cyclic amine L and three atoms O(21), O(31), and O(41), from the bridging oximate groups, are

---

(27) Chaudhuri, P.; Wieghardt, K. *Prog. Inorg. Chem.* **1987**, *35*, 329.

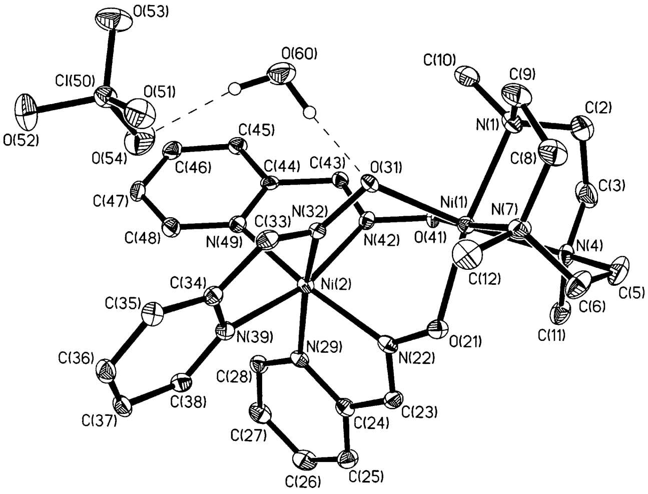

Figure 3. ORTEP diagram of complex $[LNi^{II}Ni^{II}(PyA\text{-}H)_3](ClO_4)\cdot H_2O$ (**3a**).

Table 4. Selected Bond Lengths (Å) and Angles (deg) for Complex $\mathbf{3a}\cdot H_2O$

Ni···Ni	3.491		
Ni(1)−O(41)	2.0284(19)	Ni(2)−N(22)	2.023(2)
Ni(1)−O(21)	2.059(2)	Ni(2)−N(42)	2.027(2)
Ni(1)−O(31)	2.077(2)	Ni(2)−N(32)	2.040(2)
Ni(1)−N(7)	2.117(3)	Ni(2)−N(49)	2.104(3)
Ni(1)−N(4)	2.127(2)	Ni(2)−N(29)	2.114(2)
Ni(1)−N(1)	2.137(2)	Ni(2)−N(39)	2.122(2)
O(21)−N(22)	1.326(3)	N(32)−C(33)	1.289(4)
N(22)−C(23)	1.297(4)	O(41)−N(42)	1.335(3)
O(31)−N(32)	1.338(3)	N(42)−C(43)	1.289(3)
O(41)−Ni(1)−O(21)	95.38(8)	N(22)−Ni(2)−N(29)	78.69(10)
O(41)−Ni(1)−O(31)	94.17(8)	N(42)−Ni(2)−N(29)	102.06(9)
O(21)−Ni(1)−O(31)	95.86(8)	N(32)−Ni(2)−N(29)	163.99(9)
O(41)−Ni(1)−N(7)	171.97(9)	N(49)−Ni(2)−N(29)	92.91(10)
O(21)−Ni(1)−N(7)	89.21(9)	N(22)−Ni(2)−N(39)	100.90(10)
O(31)−Ni(1)−N(7)	91.91(9)	N(42)−Ni(2)−N(39)	163.22(9)
O(41)−Ni(1)−N(4)	89.60(8)	N(32)−Ni(2)−N(39)	78.19(9)
O(21)−Ni(1)−N(4)	90.10(9)	N(49)−Ni(2)−N(39)	93.50(10)
O(31)−Ni(1)−N(4)	172.62(9)	N(29)−Ni(2)−N(39)	92.96(8)
N(7)−Ni(1)−N(4)	83.80(10)	N(22)−O(21)−Ni(1)	112.14(16)
O(41)−Ni(1)−N(1)	91.10(9)	C(23)−N(22)−O(21)	119.5(3)
O(21)−Ni(1)−N(1)	170.39(9)	C(23)−N(22)−Ni(2)	117.0(2)
O(31)−Ni(1)−N(1)	90.72(9)	O(21)−N(22)−Ni(2)	123.48(17)
N(7)−Ni(1)−N(1)	83.57(10)	N(32)−O(31)−Ni(1)	110.10(15)
N(4)−Ni(1)−N(1)	82.85(10)	C(33)−N(32)−O(31)	119.1(2)
N(22)−Ni(2)−N(42)	89.47(9)	C(33)−N(32)−Ni(2)	116.6(2)
N(22)−Ni(2)−N(32)	89.80(9)	O(31)−N(32)−Ni(2)	124.27(17)
N(42)−Ni(2)−N(32)	88.79(9)	N(42)−O(41)−Ni(1)	113.20(15)
N(22)−Ni(2)−N(49)	163.62(9)	C(43)−N(42)−O(41)	119.2(2)
N(42)−Ni(2)−N(49)	78.46(9)	C(43)−N(42)−Ni(2)	117.1(2)
N(32)−Ni(2)−N(49)	100.85(9)	O(41)−N(42)−Ni(2)	123.53(17)

the donor atoms for the six-coordinated Ni(1) center, NiN_3O_3 (Figure 3). The Ni(1)−N (average = 2.127 ± 0.01 Å) and Ni(1)−O (average = 2.055 ± 0.02 Å) distances correspond to those of known values for Ni^{II} complexes with this macrocyclic amine[28] and are in agreement with a d^8 high-spin electronic configuration, which is also fully supported by the magnetochemical results. A deviation from the idealized 90° interbond angles is found within the five-membered N−Ni(1)−N chelate rings, with the N−Ni(1)−N angles ranging between 82.9(1)° and 83.8(1)°, whereas the O−Ni(1)−O angles in the six-membered rings fall between 94.2(1) and 95.9(1)°. The coordinated macrocyclic amine L does not exhibit any unexpected features and hence does not warrant further discussion. The $Ni(2)(PyA\text{-}H)_3$ fragment of complex **3a** with a twist angle of 40.3° is very similar to those of other complexes described here.

The molecular structures of the cations in **3b**, **3c**, and **4** are shown in Figures S1, S2, and S3 (Supporting Information), respectively, and Table S1 (Supporting Information) lists selected bond distances and angles for complex **4**.

In the heterodinuclear complex $Zn^{II}Ni^{II}$ (**5**), Zn(1) is coordinated to the macrocyclic amine and O atoms of the tris(pyridine-2-aldoximato)nickel(II) monoanionic ligand, yielding a six-coordinated ZnN_3O_3. The metrical parameters for Zn(1)−O and Zn(1)−N distances with 2.083 and 2.215 Å, respectively, are very similar to those reported for dinuclear Zn^{II} complexes with this macrocyclic amine[29] and for similar oxime-containing complexes.[4,30] The $Ni(PyA)_3^-$ unit with a twist angle of 41° is very similar to that described before. Figure 4 shows the structure of the dinuclear monocation in **5**; Table 5 lists selected bond distances and angles. The trigonal distortions of the Ni center in the $Ni(PyA)_3^-$ fragment, expressed as twist angle ψ and dihedral angle θ, are listed in Table 6 for comparison purposes. Table 6 clearly exhibits the small but significant influence of the heterometal atom on the trigonal distortion of the $Ni(oximato)_3^-$ unit.

Molecular Structure of $\mathbf{6\cdot 3CH_3OH\cdot 3H_2O}$. Figure S4 (Supporting Information) displays the structure of the monocation, and Table S2 (Supporting Information) summarizes selected bond distances and angles.

Each Zn ion in the dinuclear monocation is in a distorted octahedral ligand environment, one having a $Zn(2)N_3O_3$ coordination sphere and the other with a $Zn(1)N_6$ coordination sphere, which are very similar to those reported[29] for Zn^{II} complexes with this macrocyclic amine, and similar analogous $[LFe^{III}(PyA\text{-}H)_3Zn]^{2+}$ and $[LCr^{III}(PyA\text{-}H)_3Zn]^{2+}$ oxime-containing complexes[4] including complex **5** described above. That the array Zn(1)(N−O)Zn(2) is not planar is shown by the dihedral angle θ of 40.1° between the planes comprising Zn(1)(N−O) and Zn(2)(O−N) atoms. The nonbonding intramolecular Zn···Zn distance in **6** is at 3.595 Å. This metal···metal distance is at 3.491 Å in the Ni^{II}_2 dinuclear complex **3a**.

Magnetic Susceptibility and EPR Measurements. Magnetic susceptibility data for polycrystalline samples of the complexes were collected in the temperature range 2−290 K in an applied magnetic field of 1 T. Because complex **5** contains only one paramagnetic center, viz., Ni^{II}, it is magnetically mononuclear and accordingly exhibits essentially temperature-independent μ_{eff} values of 2.93 ± 0.03

---

(28) Chaudhuri, P.; Küppers, H.-J.; Wieghardt, K.; Gehring, S.; Haase, W.; Nuber, B.; Weiss, J. *J. Chem. Soc., Dalton Trans.* **1988**, 1367.

(29) Chaudhuri, P.; Stockheim, C.; Wieghardt, K.; Deck, W.; Gregorzik, R.; Vahrenkamp, H.; Nuber, B.; Weiss, J. *Inorg. Chem.* **1992**, *31*, 1451.

(30) Burdinski, D.; Bill, E.; Birkelbach, F.; Wieghardt, K.; Chaudhuri, P. *Inorg. Chem.* **2001**, *40*, 1160.

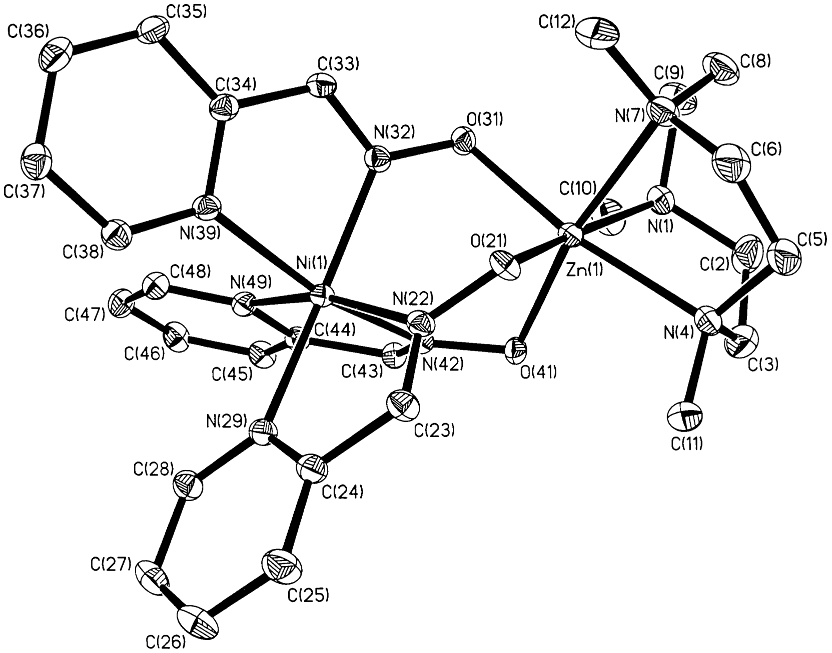

Figure 4. Molecular structure of the cation in complex [LZn^{II}Ni^{II}(PyA-H)$_3$]$^+$ (**5**).

Table 5. Selected Bond Lengths (Å) and Angles (deg) for Complex **5**

Zn···Ni	3.472		
Zn(1)−O(41)	2.0547(12)	Ni(1)−N(22)	2.0325(14)
Zn(1)−O(21)	2.0851(12)	Ni(1)−N(42)	2.0324(14)
Zn(1)−O(31)	2.1078(12)	Ni(1)−N(32)	2.0504(14)
Zn(1)−N(7)	2.2024(15)	Ni(1)−N(49)	2.1088(14)
Zn(1)−N(4)	2.2163(16)	Ni(1)−N(29)	2.1164(13)
Zn(1)−N(1)	2.2271(16)	Ni(1)−N(39)	2.1193(14)
O(21)−N(22)	1.3354(17)	N(32)−C(33)	1.283(2)
N(22)−C(23)	1.294(2)	O(41)−N(42)	1.3395(17)
O(31)−N(32)	1.3493(18)	N(42)−C(43)	1.294(2)
O(41)−Zn(1)−O(21)	96.52(5)	O(21)−Zn(1)−N(4)	91.07(5)
O(41)−Zn(1)−O(31)	95.44(5)	O(31)−Zn(1)−N(4)	169.93(5)
O(21)−Zn(1)−O(31)	97.07(5)	N(7)−Zn(1)−N(4)	81.47(6)
O(41)−Zn(1)−N(7)	169.31(6)	O(41)−Zn(1)−N(1)	92.01(5)
O(21)−Zn(1)−N(7)	89.40(5)	O(21)−Zn(1)−N(1)	167.82(5)
O(31)−Zn(1)−N(7)	92.65(5)	O(31)−Zn(1)−N(1)	90.74(5)
O(41)−Zn(1)−N(4)	89.50(5)		
N(7)−Zn(1)−N(1)	80.89(6)	N(32)−Ni(1)−N(39)	78.14(5)
N(4)−Zn(1)−N(1)	80.30(6)	N(49)−Ni(1)−N(39)	93.74(6)
N(22)−Ni(1)−N(42)	89.92(6)	N(29)−Ni(1)−N(39)	93.08(5)
N(22)−Ni(1)−N(32)	90.23(5)	N(22)−O(21)−Zn(1)	110.15(9)
N(42)−Ni(1)−N(32)	89.40(6)	C(23)−N(22)−O(21)	118.98(14)
N(22)−Ni(1)−N(49)	164.48(6)	C(23)−N(22)−Ni(1)	117.24(12)
N(42)−Ni(1)−N(49)	78.57(5)	O(21)−N(22)−Ni(1)	123.77(10)
N(32)−Ni(1)−N(49)	99.92(5)	N(32)−O(31)−Zn(1)	107.82(9)
N(22)−Ni(1)−N(29)	78.43(6)	C(33)−N(32)−O(31)	118.77(14)
N(42)−Ni(1)−N(29)	101.21(5)	C(33)−N(32)−Ni(1)	116.59(12)
N(32)−Ni(1)−N(29)	164.35(6)	O(31)−N(32)−Ni(1)	124.63(10)
N(49)−Ni(1)−N(29)	93.50(6)	N(42)−O(41)−Zn(1)	111.11(9)
N(22)−Ni(1)−N(39)	99.86(6)	C(43)−N(42)−O(41)	118.42(14)
N(42)−Ni(1)−N(39)	164.10(5)		

Table 6. Trigonal Distortion of the [Ni(oximate)$_3$]$^-$ fragment in Complexes **1**−**5**, **7**, and **8**

complex	Fe^{III}···Ni^{II}, Ni^{II}···Ni^{II}, or Zn^{II}···Ni^{II} (Å)	av twist angle ψ (deg)[a]	dihedral angle θ (deg)[b]
Ni^{II}Fe^{III}Ni^{II} (**1**)	3.545	40.0	38.4
Mn^{III}Ni^{II} (**2**)	3.506	39.3	39.8/44.2/39.0
Ni^{II}Ni^{II} (**3a**)	3.491	40.4	41.3/44.3/43.7
Ni^{II}Ni^{II} (**3b**)	3.434	40.1	35.8/40.4/41.8
Ni^{II}Ni^{II} (**3c**)	3.423	43.4	46.8/46.8/46.8
Ni^{II}Ni^{II} (**4**)	3.554	38.3	38.5/38.7/30.0
Zn^{II}Ni^{II} (**5**)	3.472	41.3	43.9/44.9/41.8
Ni^{II}Mn^{III}Ni^{II} (**7**)[16]	3.570	38.0	36.5
Ni^{II}Cr^{III}Ni^{II} (**8**)[16]	3.552	36.9	35.2

[a] The trigonal twist angle ψ is the angle between the triangular faces comprising N(29)−N(39)−N(49) (i.e., three pyridine N atoms) and N(22)−N(32)−N(42) (i.e., azomethine N atoms) and has been calculated as the mean of the Newman projection angles viewed along the centroid of focus. For an ideal trigonal-prismatic arrangement, ψ is 0° and 60° for an octahedron (or trigonal antiprism). [b] That the core Ni(N−O)M is not planar is shown by the dihedral angles θ between the planes comprising Ni(N−O) and M(O−N) atoms.

μ_B for $T > 20$ K. Simulations of the experimental magnetic moment data yield a g_{Ni} value of 2.062 with $S_{Ni} = 1$ and $S_{Zn} = 0$ for **5**.

For complexes **1**−**4**, we use the Heisenberg spin Hamiltonian in the form

$$H = -2J(S_1 \cdot S_2 + S_2 \cdot S_3) + \sum g_i \mu_B S_i \cdot B$$

for isotropic exchange coupling with $S_1 = S_3 = S_{Ni} = 1$ and $S_2 = S_{Fe} = {}^5/_2$ for **1**, $S_1 = S_{Mn} = 2$, $S_2 = S_{Ni} = 1$, and $S_3 = 0$ for **2**, and $S_1 = S_2 = S_{Ni} = 1$ and $S_3 = 0$ for **3a**−**c** and **4**. The experimental data as the effective magnetic moments (μ_{eff}) vs temperature (T) are displayed in Figures 5 and 6. The experimental magnetic data were simulated using the least-squares fitting computer program *Julx*[31] with a full-matrix diagonalization approach, and the solid lines in Figures 5 and 6 represent the simulations.

The magnetic moment μ_{eff} for **1**, Ni^{II}Fe^{III}Ni^{II}, of 5.26 μ_B ($\chi_M T = 3.465$ cm^3·K·mol^{-1}) at 290 K decreases monotonically with decreasing temperature until it reaches a value of 1.77 μ_B ($\chi_M T = 0.3916$ cm^3·K·mol^{-1}) at 30 K. Because of normal field saturation, the magnetic moment decreases further and reaches a value of 1.37 μ_B ($\chi_M T = 0.2346$

---

(31) Bill, E. *Max-Planck-Institut für Bioanorganische Chemie*: Mülheim an der Ruhr, Germany, 2005.

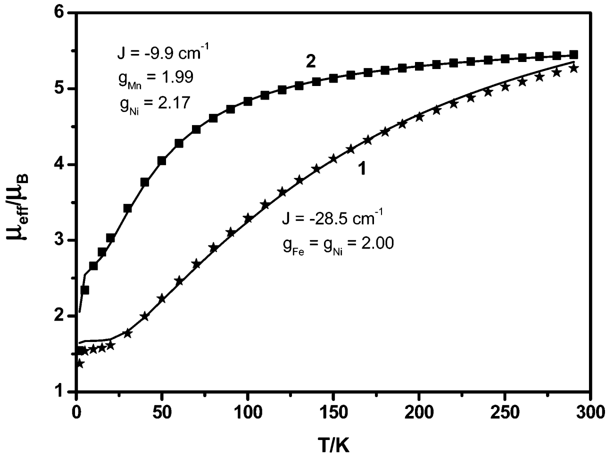

Figure 5. Plots of μ_{eff} vs T for complexes **1** and **2**. The solid lines represent the simulations using the parameters given in the text.

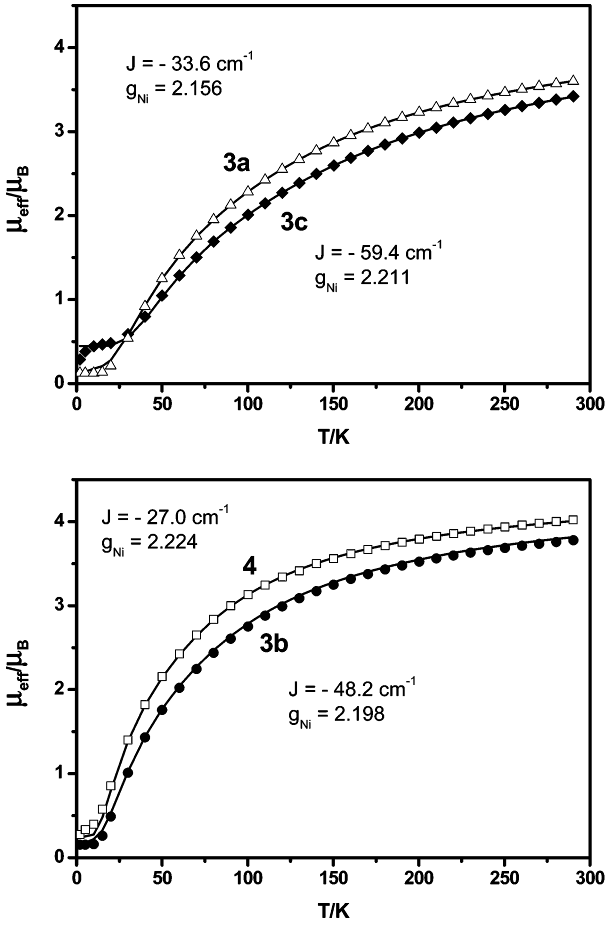

Figure 6. Simulated (solid lines) and experimental data for the μ_{eff} vs T plots of complexes **3a**−**c** and **4**.

$cm^3 \cdot K \cdot mol^{-1}$) at 2 K. This temperature dependence is in agreement with a moderate antiferromagnetic coupling between the neighboring Ni^{II} and Fe^{III} ions, resulting in an $S_t = {}^1/_2$ ground state for **1**. The temperature dependence of μ_{eff} was well simulated, shown as a solid line in Figure 5, with parameters $J = -28.5$ cm^{-1} and $g_{\mathrm{Fe}} = g_{\mathrm{Ni}} = 2.00$. The observed antiferromagnetic coupling agrees well with the comparable exchange-coupling constants reported earlier.[4,9,13]

Because g_{Ni} is generally expected to be greater than 2.0, we attempted to fit the experimental data for **1** with g_{Ni} other than 2.0, but without any success; all fittings were of poor quality. Moreover, g values cannot be evaluated accurately from the bulk susceptibility measurements. Hence, we prefer the parameters reported above.

The magnetic behavior of Mn^{III}Ni^{II} (**2**) is characteristic of an antiferromagnetic coupling of $S_{\mathrm{Mn}} = 2$ and $S_{\mathrm{Ni}} = 1$ in the dinuclear complex. At 290 K, the μ_{eff} value of 5.45 μ_B ($\chi_M T$ = 3.707 $cm^3 \cdot K \cdot mol^{-1}$) decreases monotonically with decreasing temperature until it reaches a value of 2.85 μ_B ($\chi_M T$ = 1.013 $cm^3 \cdot K \cdot mol^{-1}$) at 15 K, below which it drops rapidly to 1.545 μ_B ($\chi_M T = 0.2983$ $cm^3 \cdot K \cdot mol^{-1}$) at 2 K. Below 15 K, the decrease in μ_{eff} may be due to the zero-field splitting of the ground state $S_t = 1$, expected from an antiferromagnetic coupling between two paramagnetic centers of $S_{\mathrm{Mn}} = 2$ and $S_{\mathrm{Ni}} = 1$. The temperature dependence of μ_{eff} was well simulated with parameters $J_{\mathrm{MnNi}} = -9.9$ cm^{-1}, $g_{\mathrm{Mn}} = 1.99$, $g_{\mathrm{Ni}} = 2.17$, and $|D| = 4.1$ cm^{-1}, and the simulation is shown as a solid line in Figure 5. It is to be noted that the antiferromagnetic interaction operating in **2** is stronger than that in Ni^{II}Mn^{III}Ni^{II} (**7**)[19a] irrespective of the nearly identical Ni···Mn distances [3.57 Å (**7**) vs 3.51 Å (**2**)]. We attribute this to more covalence in the three Mn−N and three Mn−O bonds together with the distortion of the Mn center for **2** in comparison to that for only six Mn−O bonds in **7**. *This result also underlines the importance of nonbridging ligands in determining the strength of exchange-coupling interactions.*

The magnetic moment μ_{eff}/molecule for Ni^{II}Ni^{II}(PyA-H)$_3$ (**3a**) of 3.78 μ_B ($\chi_M T$ = 1.787 $cm^3 \cdot K \cdot mol^{-1}$) at 290 K is much smaller than the "spin-only" value of 4.00 μ_B for two uncoupled Ni^{II} ions of spin $S = 1.0$. The magnetic moment decreases with decreasing temperature, reaching a value of 0.086 μ_B ($\chi_M T = 0.937 \times 10^{-3}$ $cm^3 \cdot K \cdot mol^{-1}$) at 2 K, which is a clear indication of an antiferromagnetic exchange coupling between two paramagnetic centers Ni^{II} ($S_{\mathrm{Ni}} = 1$) with a resulting diamagnetic ground state. The solid line in Figure 6 represents the best fit with the following parameters: $J = -33.6$ cm^{-1}, $g_{\mathrm{Ni}} = 2.156$, and 0.2% PI, paramagnetic impurity ($S = 1.0$). Figure 6 also represents the μ_{eff} vs T plots for Ni^{II}Ni^{II}(PyA-Me)$_3$ (**3b**), Ni^{II}Ni^{II}(PyA-Ph)$_3$ (**3c**), and Ni^{II}Ni^{II}(MeImA)$_3$ (**4**), together with their simulations as the solid lines. The following best-fit parameters are evaluated: $J = -48.2$ cm^{-1}, $g_{\mathrm{Ni}} = 2.198$, and PI = 0.3% for **3b**, $J = -59.4$ cm^{-1}, $g_{\mathrm{Ni}} = 2.211$, PI = 2.5% for **3c**, and $J = -27.0$ cm^{-1}, $g_{\mathrm{Ni}} = 2.224$, and PI = 0.8% for **4**. Thus, the strength of the exchange coupling follows the order **3c** > **3b** > **3a** > **4**, indicating that *the substituents on the aldehydic C can influence the strength of the exchange coupling.* Additionally, a comparison of the magnetic behavior of **3a** with that of **4** reveals the stronger σ-donor ability of the pyridine N than that of the imidazole N. The variation in the strength of the exchange couplings within these four dinuclear Ni^{II} complexes can be qualitatively correlated to (i) the Ni−N$_{\mathrm{oxime}}$ bond lengths, (ii) the nonbonding Ni(1)···Ni(2) distances, and (iii) the distortion of the trigonal prism to the octahedron of the Ni^{II}(oximate)$_3$ unit, which enhances the antiferromagnetic exchange coupling by making the magnetic orbitals' overlap favorable. For establishing magnetostructural correlations for such Ni$^{II}_2$

complexes, more oximato-bridged paramagnetic complexes of Ni^{II} are thus warranted. To date, only a few structurally characterized oximato-bridged homometal Ni^{II} complexes have been subjected to magnetic susceptibility measurements to evaluate the nature of exchange coupling; the antiferromagnetic exchange-coupling constant exhibits a wide variation, -7 cm^{-1} $> J > -80$ cm^{-1}. Although **3a**−**c** and **4** are the only known triply oximato-bridged Ni$^{II}_2$ complexes, their *J* values lie well within the range reported in the literature.[13,32]

Considering the O and N atoms of the bridging oximato groups as sp^2-hybridized in the network Ni(O−N)$_3$Ni or Mn(O−N)$_3$Ni, the nature of the exchange interactions between the spin carriers can be rationalized on the basis of the established Goodenough−Kanamori rules[33] for superexchange as presented concisely by Ginsberg[34] and later by Kahn[3] within the framework of localized spins. Thus, the following dominant interactions of the sp^2 orbitals (oxime N and O atoms) on either side of the bridging oximate can be envisaged for the Ni^{II}Ni^{II} pair, present in complexes **3a**−**c** and **4**

$$\mathrm{d}_{x^2-y^2}||\sigma_{\mathrm{sp}}{}^2(\mathrm{NO})||\mathrm{d}'_{x^2-y^2} \qquad \text{antiferromagnetic}$$

$$\mathrm{d}_{z^2}||\sigma_{\mathrm{sp}}{}^2(\mathrm{NO})||\mathrm{d}'_{z^2} \qquad \text{weak antiferromagnetic}$$

$$\mathrm{d}_{x^2-y^2}||\sigma_{\mathrm{sp}}{}^2(\mathrm{NO})\perp\mathrm{d}'_{z^2} \qquad \text{ferromagnetic}$$

which lead to an overall exchange interaction as antiferromagnetic and whose strength is expected to be much weaker than that for the oximato-bridged Cu$^{II}_2$ complexes. This is in complete accordance with the reported values for the oximato-bridged Ni^{II} [13,32] and Cu^{II} [35] complexes. Similarly, the superexchange pathway e$_g$(Ni)||σ_{NO}||e′$_g$(Fe) determines the sign of *J* for the Fe^{III}Ni^{II} pair in complex **1**. On the other hand, d$_{z^2}$(Mn^{III})||σ_{NO}||d′$_{z^2}$(Ni^{II}) is determinant for the sign of the exchange coupling for the Mn^{III}Ni^{II} pair in complexes **2** and **7**.

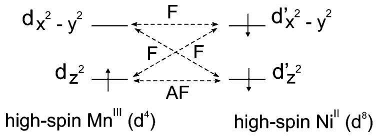

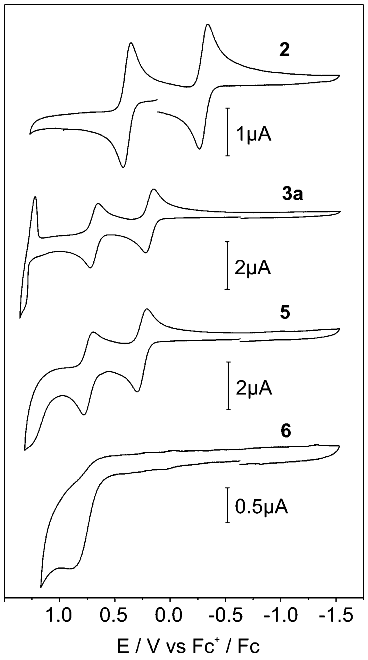

Figure 7. Cyclic voltammograms of complexes **2**−**6** recorded in CH$_2$Cl$_2$ solutions containing 0.1 M [(*n*-Bu)$_4$N]PF$_6$ as the supporting electrolyte at ambient temperatures and a scan rate of 100 mV s^{-1}. A glassy carbon working electrode (0.03 cm^2) was used, and potentials are referenced versus the Fc$^+$/Fc couple.

Table 7. Formal Electrode Potentials for Oxidation and Reduction (in V vs Fc$^+$/Fc) of Complexes **2**−**5** [Measured at Ambient Temperatures in CH$_2$Cl$_2$ Solutions Containing 0.1 M [(*n*-Bu)$_4$N]PF$_6$][a]

complex	oxidation	oxidation	oxidation	reduction
[LMn^{III}(PyA-H)$_3$Ni^{II}]$^{2+}$ (**2**)	+1.43 m	+0.38		−0.30
[LNi^{II}(PyA-H)$_3$Ni^{II}]$^+$ (**3a**)	+1.29	+0.69	+0.18	
[LNi^{II}(PyA-Me)$_3$Ni^{II}]$^+$ (**3b**)	+1.14	+0.59	+0.055	
[LNi^{II}(PyA-Ph)$_3$Ni^{II}]$^+$ (**3c**)	+1.28	+0.62	+0.066	
[LNi^{II}(MeImA)$_3$Ni^{II}]$^+$ (**4**)		+0.58	+0.11	
[LZn^{II}(PyA-H)$_3$Ni^{II}]$^{1+}$ (**5**)	+1.27 irr	+0.74	+0.25	
[LZn^{II}(PyA-H)$_3$Zn^{II}]$^{1+}$ (**6**)	+0.90 irr			

[a] m: measured in CH$_3$CN. irr: redox process is irreversible; peak potentials are given.

Electrochemistry. Cyclic voltammograms of complexes **2**−**6** have been recorded in CH$_2$Cl$_2$ solutions containing 0.1 M [(*n*-Bu)$_4$N]PF$_6$. A conventional three-electrode arrangement was used, consisting of a glassy carbon working electrode, a Ag/AgNO$_3$ reference electrode, and a Pt wire counter electrode. Ferrocene was added as an internal standard after completion of a set of experiments, and potentials are referenced vs the ferrocenium/ferrocene (Fc$^+$/Fc) couple. The cyclic voltammograms of the complexes are shown in Figure 7, and the redox potentials obtained from the voltammograms are presented in Table 7.

Coulometric experiments for the reversible redox processes were performed (at −25 °C) at appropriate potentials to determine the number of electrons/molecule transferred in the process. It was found that all reversible CV waves represent one-electron oxidations (with **2**, there is additionally a one-electron reduction). For EPR analysis, after completion of coulometry, samples of the fully oxidized or reduced forms were transferred into EPR tubes and frozen to liquid-nitrogen temperature.

Complex Zn^{II}Zn^{II} (**6**) contains only redox-inactive Zn^{II} metal ions, and its cyclic voltammogram exhibits only one irreversible oxidation at +0.93 vs Fc$^+$/Fc. Clearly, this

---

(32) (a) Agnus, Y.; Louis, R.; Jesser, R.; Weiss, R. *Inorg. Nucl. Chem. Lett.* **1976**, *12*, 455. (b) Fauss, J.; Lloret, F.; Julve, M.; Clemente-Juan, J. M.; Munoz, M.; Solans, X.; Font-Bardia, M. *Angew. Chem., Int. Ed. Engl.* **1996**, *35*, 1485. (c) Pavlishchuk, V. V.; Kolotilov, S. V.; Addison, A. W.; Prushan, M. J.; Butcher, R. J.; Thompson, L. K. *Inorg. Chem.* **1999**, *38*, 1759. (d) Pavlishchuk, V. V.; Kolotilov, S. V.; Addison, A. W.; Prushan, M. J.; Schollmeyer, D.; Thompson, L. K.; Goreshnik, E. A. *Angew. Chem., Int. Ed. Engl.* **2001**, *40*, 4734. (e) Pavlishchuk, V. V.; Birkelbach, F.; Weyhermüller, T.; Wieghardt, K.; Chaudhuri, P. *Inorg. Chem.* **2002**, *41*, 4405. (f) Khanra, S.; Weyhermüller, T.; Rentschler, E.; Chaudhuri, P. *Inorg. Chem.* **2005**, *44*, 8176.

(33) (a) Goodenough, J. B. *Magnetism and the Chemical Bond*; Wiley: New York, 1963. (b) Goodenough, J. B. *J. Phys. Chem. Solids* **1958**, *6*, 287. (c) Kanamori, J. *J. Phys. Chem. Solids* **1959**, *10*, 87.

(34) Ginsberg, A. P. *Inorg. Chim. Acta Rev.* **1971**, *5*, 45.

(35) A comprehensive list of *J* values for oximato-bridged polynuclear copper(II) complexes are given in ref 13 (see Table 1).

oxidation must occur at the ligand system. Because the triazacyclononane ligand L is known not to be oxidizable in this potential range,[27] the oxidation must be due to the (irreversible) oxidation of the pyridine-2-aldoxime moiety in the PyA-H ligand.

Complex $Zn^{II}Ni^{II}$ (**5**) is composed of the Ni-containing $Ni^{II}(PyA\text{-}H)_3^-$ unit, ligated to the redox-inert LZn^{II}. Here, an irreversible oxidation (at $+1.27$ V; again assigned to the PyA oxidation) is preceded by two reversible oxidations at $+0.25$ and $+0.74$ V vs Fc^+/Fc. These additional reversible oxidations must both arise from the Ni^{II} ion of the $Ni^{II}(PyA)_3^-$ ligand. Hence, they represent a successive, stepwise oxidation of the Ni to its Ni^{III} form and then to its Ni^{IV} form. It is known that oxime ligands[14] stabilize high-valent Ni oxidation states, and the EPR spectrum (see the EPR of Electrogenerated Species section) confirms indeed that the reversible oxidations are Ni-centered, unless a Mn ion is present.

Complex $Ni^{II}Ni^{II}$ (**3a**) carries an additional Ni ion in LNi^{II} and thus a further oxidizable site. It shows two reversible oxidations (0.18 and 0.69 V vs Fc^+/Fc) at potentials similar to those observed with **5**. Clearly, the oxidations are Ni-centered, and the similarity of the potentials of **3a**−**c** and **4** suggests that they occur at $(PyA)_3Ni^{II}$, the common structural element of **3a**−**c** and **4**. This is fully confirmed by the EPR measurements (see the EPR of Electrogenerated Species section). Therefore, the alternative mechanism of a Ni oxidation at LNi^{II} can be ruled out, and the oxidations are unambiguously assigned to Ni-based oxidations at $(PyA)_3Ni^{II}$, yielding $[LNi^{II}(oxime)_3Ni^{III}]^{2+}$ and $[LNi^{II}(oxime)_3Ni^{IV}]^{3+}$ species. This confirms once more that aldoximes stabilize high-valent Ni centers better than other ligands, in our case better than ligand L. An additional third oxidation is discernible at $+1.29$ V, close to the border of the accessible potential range of CH_2Cl_2. Because after oxidation a reverse, re-reduction peak is clearly visible, this oxidation is (chemically) reversible, in contrast to the ligand-centered oxidation observed with **5** and **6**. Therefore, we assign it to the oxidation of the Ni^{II} ion in LNi^{II} to LNi^{III}. The symmetric and narrow shape of the reverse wave of the oxidation is typical for a “stripping” peak and indicates that complexes **3** and **4** after the third oxidation, being then a tetracation $[LNi^{III}(oxime)_3Ni^{IV}]^{4+}$, are no longer soluble in CH_2Cl_2 and rapidly deposit on the surface of the working electrode.

The Mn^{III}-containing complex **2** is a *di*cation, in contrast to the *mono*cationic compounds **3**−**5**. Therefore, if the *first* oxidation of **2** is Ni-centered, it should occur at potentials close to those of the *second* oxidation of **3a**−**c** and **4**, i.e., around $+0.65$ V. However, it occurs at significant lower potentials, at $+0.38$ V. Therefore, we assign it to the oxidation $LMn^{III} \rightarrow LMn^{IV}$, which is again confirmed by the EPR measurements (see the EPR of Electrogenerated Species section). The reduction of **2** at -0.30 V is assigned to the Mn^{III}/Mn^{II} couple because the alternative formation of Ni^{I} does not appear feasible under such mild reducing potentials and it was not observed with complexes **3a**−**c** and **4**. This assignment is again in accordance with the EPR measurements. One might expect a Ni-centered oxidation $[(PyA)_3Ni^{II} \rightarrow (PyA)_3\,Ni^{III}]$ as a *second* oxidation step of **2**, at potentials where the *third* oxidation occurred with **3** (i.e., at around $+1.3$ V). It was not found within the usable potential range of CH_2Cl_2 (<1.3 V vs Fc^+/Fc); however, in CH_3CN, we detected a reversible oxidation at $+1.43$ V, which is assignable to the above Ni-centered oxidation process.

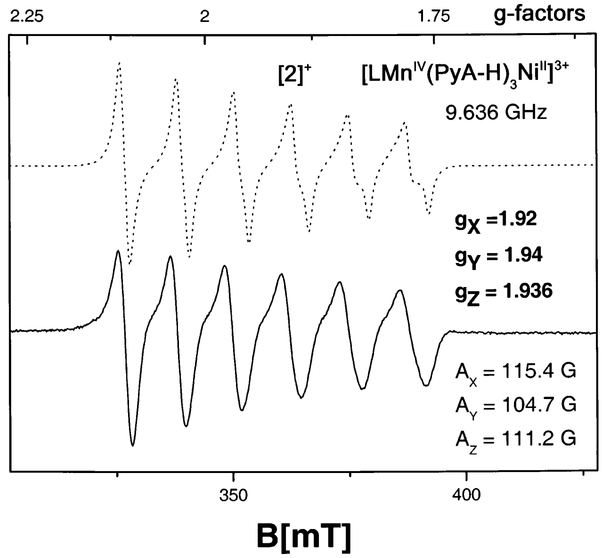

Figure 8. X-band EPR spectrum of oxidized **2**, $[\mathbf{2}]^+$, in CH_2Cl_2/toluene (1:1) at 10 K. Experimental parameters: frequency 9.64 GHz, power 10 μW, modulation 1 mT. The dotted line is a spin Hamiltonian simulation for total spin $S_t = {}^1/_2$ with parameters given in the text.

EPR of Electrogenerated Species. The one-electron-oxidized product $[\mathbf{2}]^+$ of $Mn^{III}Ni^{II}$ (**2**) obtained by coulometric experiments in CH_2Cl_2/toluene (1:1) was subjected to X-band EPR spectroscopy at low temperatures. Figure 8 presents the derivative spectrum of $[\mathbf{2}]^+$ at 10 K and its simulation.

The EPR spectrum exhibiting well-resolved sextets of the characteristic ^{55}Mn hyperfine lines ($I = {}^5/_2$) clearly indicates a $S = {}^1/_2$ powder pattern, resulting from the antiferromagnetic interaction between the Mn^{IV} ($S = {}^3/_2$) and Ni^{II} ($S = 1$) centers of the oxidized species, $[\mathbf{2}]^+$. This is in complete accordance with the assignment of the Mn^{III}-centered oxidation (see the Electrochemistry section) of the starting compound **2** containing the $Mn^{III}Ni^{II}$ core. The alternative assignment of the Ni^{II}-centered oxidation should have led to a ground state of $S = {}^3/_2$, or ${}^5/_2$ arising from spin-exchange interactions between the spins of the oxidized species Mn^{III}-Ni^{III} with $S_{Mn^{III}} = 2$ and $S_{Ni^{III}} = {}^1/_2$. The simulation obtained with the spin Hamiltonian parameters, $g_x = 1.92$, $g_y = 1.94$, $g_z = 1.936$, $A_x = 115.4$ G, $A_y = 104.7$ G, and $A_z = 111.2$ G, is shown as the dotted line in Figure 8. The g values smaller than 2.00 indicate the dominance of g_{Mn} over g_{Ni}, as is also in conformation with the spin-projection coefficients, $g = (5/3)g_{Mn} - (2/3)g_{Ni}$ (with $g_{Ni} > 2$).

The second oxidation of **2**, $[\mathbf{2}]^{2+}$, performed in CH_3CN leads to an EPR-silent species due to an integer-spin system ($S = 1$ or 2). No further characterization of the putative Ni^{IV} in $[\mathbf{2}]^{2+}$ was performed.

The electrooxidized species of **5**, resulting in $[LZn^{II}(PyA\text{-}H)_3Ni^{III}]^{2+}$, provided EPR spectra at both X and Q bands, shown in Figure 9.

The assignment from the electrochemical measurements of the formation of the Ni^{III} center in $[\mathbf{5}]^+$ is fully cor-

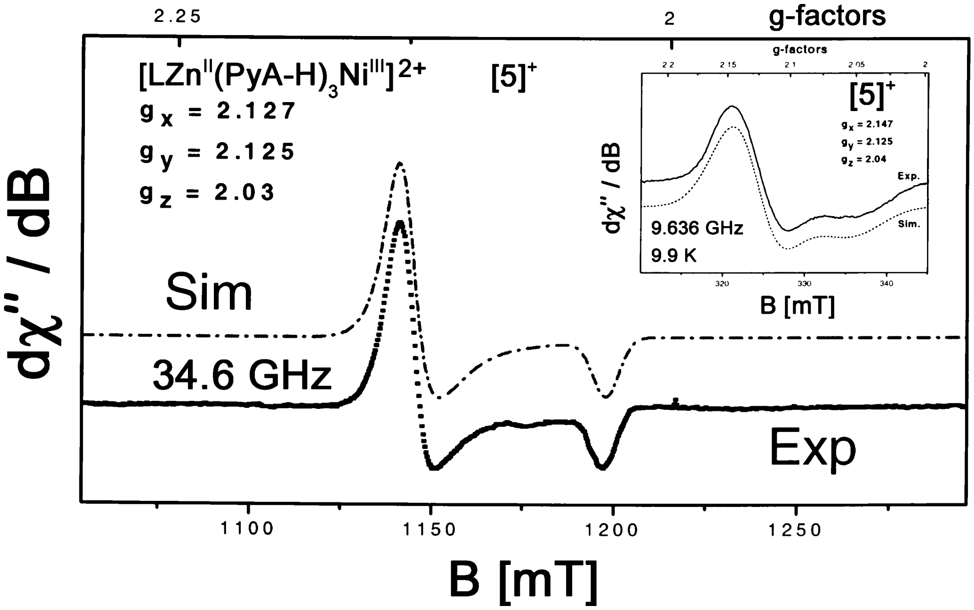

Figure 9. Q- and X-band (inset) EPR spectra of $[\mathbf{5}]^+$ in CH_2Cl_2/toluene (1:1) at 10 K.

roborated with the EPR measurements. The EPR spectra clearly show the low-spin character of Ni^{III} d^7 in $[\mathbf{5}]^+$.[36] The Q-band spectrum is virtually axial with three principal g values of 2.127, 2.125, and 2.03. At the X band, the spectrum (inset of Figure 9) is rather broad, presumably because of intermolecular interactions. The average g value, $\langle g \rangle = 2.094$, indicates that the unpaired electron is associated primarily with the Ni ion and not with the ligand. The present behavior with $g_\perp > g_\parallel$ is consistent with a d_{z^2} ground state in a tetragonally distorted octahedral geometry with elongation of the axial bonds. Thus, upon removal of an electron from the Ni^{II} center in **5**, there is a structural change.

That the first electrochemical oxidation of **3a**−**c** and **4** provides a mixed-valent $Ni^{II}Ni^{III}$ species, in which the Ni^{III} center is associated only with the oxime N atoms, has also been checked by the EPR measurements at helium temperatures. As a prototype of complexes **3** and **4**, we have chosen complex **3c**, containing the phenyl derivative of the ligand pyridine-2-aldoxime, PyA-Ph, for the coulometric experiments, and the electrooxidized species $[\mathbf{3c}]^+$ was subjected to EPR measurements.

The X-band EPR spectrum of $[\mathbf{3c}]^+$ measured in a frozen solution at liquid-helium temperatures shows the superposition of an asymmetric derivative signal with shoulders and satellite lines centered at $g \approx 2.2$ and a broad low-field peak at about $B = 165$ mT (Figure 10).

The high g factor of the latter signal, $g \approx 4$, is typical of a spin quartet species with large zero-field splitting and axial symmetry ($|D| \gg h\nu$ and $E/D \approx 0$). In this situation, the effective $g_{x,y}$ values of the $|S = {}^3/_2, m_s = \pm{}^1/_2\rangle$ Kramers doublet are equal to the value of $2S + 1$, whereas g_z is at 2. Moreover, the $|S = {}^3/_2, m_s = \pm{}^3/_2\rangle$ Kramers doublet is then extremely anisotropic and virtually EPR-silent. In fact, the actual derivative signal at $g = 4$ as well as its contribution in the absorption spectrum obtained by numerical integration (inset of Figure 10) could be very well simulated with spin $S = {}^3/_2$ and the parameters $g = (2.053, 2.053, 2.1)$, $D = 1$ cm^{-1} (or any higher value), and $E/D = 0.07$ (solid lines). A Gaussian distribution of the rhombicity parameter with half-width $\sigma(E/D) = 0.09$ and a frequency-dependent line width $\Gamma_\nu = 12$ mT (fwhm at $g = 2$) were applied to account for the correct shape of the powder spectrum. This component of the experimental spectrum must arise from the total spin quartet state, $S_t = {}^3/_2$, of the coupled system Ni^{II}, $S_1 = 1$, and Ni^{III}, $S_2 = {}^1/_2$. Because it is thermally populated at 4.7 K, the exchange coupling constant apparently is either positive or very weak.

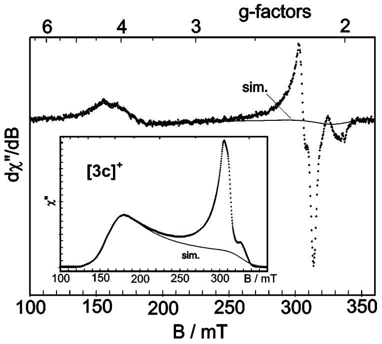

Figure 10. X-band EPR spectrum of one-electron-oxidized $[\mathbf{3c}]^+$ measured at 4.5 K (frequency 9.439924 GHz, power 200 μW, modulation 2 mT/200 kHz). The inset shows the absorption spectrum obtained by numerical integration (dots). The thin solid lines are the result of a simulation for $S_t = {}^3/_2$, with $g = (2.053, 2.053, 2.1)$, $D = 1$ cm^{-1}, $E/D = 0.07$, and a Gaussian distribution of the rhombicity parameter with half-width $\sigma(E/D) = 0.09$ and frequency-dependent line width $\Gamma_\nu = 12$ mT (fwhm at $g = 2$). The intensity of the simulated absorption spectrum accounts for 65% of the total intensity of the experimental absorption spectrum.

One might speculate that the more complex signals centered at $g \approx 2.2$ represent the corresponding total spin doublet, $S_t = {}^3/_2$, of the $Ni^{II}Ni^{III}$ system. This interpretation, however, cannot be correct for the following reasons: (i) The relative intensities of the $g \approx 2.2$ signals are preparation-

---

[36] (a) Chakravorty, A. *Isr. J. Chem.* **1985**, 2599. (b) Lappin, A. G.; McAuley, A. *Adv. Inorg. Chem.* **1988**, *32*, 241. (c) Salerno, J. C. In *The Bioinorganic Chemistry of Nickel*; Lancaster, J. R., Ed.; VCH: New York, 1988; p 53.

dependent and scattered between 35% and more than 60% at 4.2 K. (ii) The temperature dependence of its relative intensity does not obey a Boltzmann law. Particularly, the intensity ratio of the two components does not approach the limit of equal population for $T \rightarrow 60$ K. (iii) The effective **g** tensor of the expected doublet species would not be at $g \approx 2.2$ for the actual ratio of exchange coupling and zero-field interaction. The shape of the quartet spectrum proves the presence of sizable zero-field splitting $D > 1$ cm^{-1} (as expected from the partial parentship of spin from Ni^{II}), whereas the appearance and thermal population of both species at 4.7 K would be possible only for weak exchange splitting on the order of kT ($\rightarrow |J| \leq 3$ cm^{-1}). In this situation, mixing of doublet and quartet wavefunctions due to competing zero-field splitting and exchange interaction would yield more anisotropic g values for the putative doublet than was observed, with all values below $g \approx 2.2$ and at least one component below $g = 2$. [The same spin system and a similar situation of intermediately strong spin coupling is encountered and was thoroughly studied for oxoferrylporphyrin cation radical complexes for which the Fe^{IV}=O unit ($S_1 = 1$) is weakly ferromagnetically coupled to the porphyrin radical, $S_2 = {}^1/_2$].[37] For these reasons, we have to infer that the signals at $g \approx 2.2$ do not originate from the excited total spin doublet of the Ni^{II}Ni^{III} spin system. We presume that unknown intermolecular spin−spin interactions perturb our EPR signal for a variable number of weakly attached molecules in our frozen solution samples. However, the good simulation of the low-field spectral component at $g \approx 4$ shows that for the unperturbed subensemble the exchange interaction is positive and gives rise to the observed quartet EPR spectrum.

Concluding Remarks

To conclude, the following points of this study deserve particular attention:

The ligation property of the metal complexes tris(pyridine-2-aldoximato)nickel(II) and tris(1-methylimidazole-2-aldoximato)nickel(II) has been explored to generate heterometal complexes such as Ni^{II}Fe^{III}Ni^{II}, Ni^{II}Mn^{III}Ni^{II}, Ni^{II}Cr^{III}Ni^{II}, Mn^{III}Ni^{II}, and Zn^{II}Ni^{II}, together with a series of homometal Ni^{II}Ni^{II} complexes. The thermodynamic stability of the in situ generated monoanions Ni(PyA)$_3^-$ and Ni(MeImA)$_3^-$, with three facially disposed pendent oxime O atoms, makes it feasible to use these complex anions as tridentate ligands for other coordinatively unsaturated metal ions.[4,19a] The exchange interaction between the central high-spin Fe^{III} and neighboring Ni^{II} is antiferromagnetic in nature, and the exchange pathway $e_g(\mathrm{Ni})||\sigma_{sp}{}^2(\mathrm{NO})||e'_g(\mathrm{Fe})$ determines the strength and sign of J for the Fe^{III}Ni^{II} pair in complex **1**. On the other hand, the $d_{z^2}(\mathrm{Mn})||\sigma_{sp}{}^2(\mathrm{NO})||d'_{z^2}(\mathrm{Ni})$ path is determinant for the sign of the exchange coupling for the Mn^{III}-Ni^{II} pair in complexes **2** and **7**.

The deliberately synthesized isostructural series of Ni$^{II}_2$ complexes **3a**−**c** and **4** clearly demonstrate the *influence of the substitution on the aldehydic C on the strength of the exchange coupling between the two Ni^{II} centers* by changing presumably the σ-donor property of the involved oxime N atoms.

Electrochemical measurements indicate the reversible oxidations of the Ni centers ligated to the oxime N atoms, generating localized mixed-valent [LNi^{II}Ni^{III}(oxime)$_3$]$^{2+}$ species from **3a**−**c** and **4**. That the spin coupling in the Ni^{II}Ni^{III} system ($S_{\mathrm{Ni^{II}}} = 1$ and $S_{\mathrm{Ni^{III}}} = {}^1/_2$) results in a total spin quartet state, $S_t = {}^3/_2$, has been confirmed by the X-band EPR measurements. On the contrary, for complex Mn^{III}Ni^{II} (**2**), the first reversible oxidation occurs at the Mn^{III} center, resulting in the [LMn^{IV}Ni^{II}(oxime)$_3$]$^{3+}$ species. The second oxidation is Ni-centered, generating the Mn^{IV}Ni^{III} species. These assignments are fully in conformation with the EPR measurements, which indicate antiferromagnetic interactions for the spin-coupled Mn^{IV}Ni^{II} ($S_{\mathrm{Mn^{IV}}} = {}^3/_2$ and $S_{\mathrm{Ni^{II}}} = 1$) system, resulting in a doublet, $S_t = {}^1/_2$, ground state.

Acknowledgment. Financial support from the Max-Planck Society and the German Research Council (DFG) is gratefully acknowledged (Project: Priority Program “Molecular Magnetismus”, Ch111/3-3). The skillful technical assistance of H. Schucht, A. Göbels, F. Reikowski, and U. Pieper is thankfully acknowledged.

Supporting Information Available: Details of the X-ray structural data for **1**−**6** and X-ray crystallographic data (CIF), ORTEP diagrams of the cations in **3b**, **3c**, **4**, and **6** as Figures S1−S4, respectively, and Tables S1 and S2 listing selected bond angles and lengths for **4** and **6**, respectively. This material is available free of charge via the Internet at http://pubs.acs.org.

IC701073J

---

(37) (a) Bill, E.; Ding, X. Q.; Bominaar, E. L.; Trautwein, A. X.; Winkler, H.; Mandon, D.; Weiss, R.; Gold, A.; Jayaraj, K.; Hatfield, W. E.; Kirk, M. L. *Eur. J. Biochem.* **1990**, *188*, 665. (b) Rutter, R.; Hager, L. P.; Dhonau, H.; Hendrich, M.; Valentine, M.; Debrunner, P. *Biochemistry* **1984**, *23*, 6809.